Non-peer reviewed **Research Article** submitted to SEISMICA

Forecasting 3D Rupture Dynamics of the Alto Tiberina Low-Angle Normal Fault, Italy

Mathilde Marchandon *[1], **Alice-Agnes Gabriel** [2], **Lauro Chiaraluce** [3], **Elisa Tinti** [4,3], **Emanuele Casarotti** [3], **James Biemiller** [5]

[1]Ludwig-Maximilians-Universität München, Munich, Germany, [2]Scripps Institution of Oceanography, UC San Diego, La Jolla, USA, [4]Sapienza University of Rome, Rome, Italy, [3]Istituto Nazionale di Geofisica e Vulcanologia, Roma, Italy, [5]USGS, Portland, Oregon, USA

Author contributions: *Conceptualization*: MM,AG,LC,ET,EC. *Methodology*: MM,AG,LC,ET,EC,JB. *Software*: MM,AG. *Validation*: MM,AG,LC,ET,EC,JB. *Formal Analysis*: MM. *Investigation*: MM. *Resources*: AG,LC. *Writing - Original draft*: MM. *Writing - Review & Editing*: MM,AG,JB,ET,EC,LC. *Visualization*: MM. *Supervision*: AG. *Project administration*: AG. *Funding acquisition*: AG,LC,EC.

Abstract The seismic potential of active low-angle normal faults (LANFs, $< 30°$ dip) remains enigmatic under Andersonian faulting theory, which predicts that normal faults dipping less than 30° should be inactive. The Alto Tiberina fault (ATF) in the northern Apennines, a partly creeping 17°-dipping LANF, has not been associated with any historical earthquakes but could potentially generate earthquakes up to Mw 7. We investigate the mechanical preconditions and dynamic plausibility of large ATF earthquakes using 3D dynamic rupture and seismic wave propagation simulations constrained by multidisciplinary data from the Alto Tiberina Near Fault Observatory (TABOO-NFO). Our models incorporate the complex non-planar ATF fault geometry, including hanging wall secondary faults and a recent geodetic coupling model. We show that potential large earthquakes (up to Mw 7.4) are mechanically viable under Andersonian extensional stress conditions if the ATF is statically relatively weak (μ_s =0.37). Large earthquakes only nucleate on favorably oriented, steeper fault sections (dip $\geq$30°), and remain confined to the coupled portion, limiting earthquake magnitude. These ruptures may dynamically trigger an intersecting synthetic branch but are unlikely to affect more distant antithetic faults. Jointly integrating fault geometry and geodetic coupling is crucial for forecasting dynamic rupture nucleation and propagation.

1 Introduction

The Andersonian theory of faulting predicts that in an extensional tectonic regime (i.e. where the maximum compressive stress σ_1 is vertical), normal faults should form at an angle of ~60° with respect to the Earth's surface (Anderson, 1905, 1951). The Anderson-Byerlee frictional fault reactivation theory also predicts that in order to reactivate a preexisting fault as a normal fault, the fault dip should fall between 40° and 80° for a static friction coefficient

---

*Corresponding author: M.Marchandon@lmu.de

μ_s ranging from 0.6 to 1 (Sibson, 1985). To the first order, these theoretical expectations seem consistent with the instrumental record, as the global compilation of large normal-faulting earthquakes (Mw>5.5) with unambiguously determined rupture planes shows that those earthquakes occur on faults dipping between 30° and 65° (Collettini and Sibson, 2001). Yet, despite both theoretical expectations and instrumental records, existing Low Angle Normal Faults (LANFs) - normal faults dipping less than 30° - have been identified worldwide (Axen, 2004; Abers, 1991; Wernicke, 1995; Collettini, 2011). Active examples of LANFs include the Mai'iu fault in Papua New Guinea (Biemiller et al., 2020a; Little et al., 2019; Mizera et al., 2019), the low-angle detachment in the Gulf of Corinth, Greece (Rietbrock et al., 1996), and the Alto Tiberina fault, Italy (Collettini and Barchi, 2002; Chiaraluce et al., 2007; Vadacca et al., 2016).

The ability of LANFs to host large earthquakes remains debated due to the paucity of such events recorded in instrumental seismic catalogs. The 1985 Mw 6.8 Woodlark Basin earthquake in Papua New Guinea is a notable exception, with one focal mechanism plane dipping at 24°, aligning with a seismically imaged LANF (Abers, 1991). Slip on the auxiliary, steeper plane would place the uplifted metamorphic core complexes on the downthrown side of the fault, supporting the low-angle fault hypothesis (Abers, 1991). The scarcity of large LANF earthquakes in the instrumental record may be due to potentially longer recurrence intervals compared to steeper-dipping normal faults. Using simple mechanical considerations, Wernicke (1995) shows that the average slip D and recurrence interval R is proportional to $1/sin(\theta)$ and $1/tan(\theta)$, respectively (with θ the dip angle). This suggests that for a given rate of horizontal extension, LANFs accommodate the deformation with fewer but larger earthquakes compared to steeper normal faults, which aligns with neotectonic studies indicating large earthquakes on several LANFs globally (e.g. Cummins et al., 2020; Biemiller et al., 2020b; Karlsson et al., 2021). For instance, paleoseismological records of the Mai'iu fault show it has hosted infrequent but significant Mw > 7 earthquakes over the past 7000 years (Biemiller et al., 2020b).

LANFs have been the center of intense debate focusing on whether these faults formed and accommodated deformation at low angles or whether they initiated and were active at steep angles before being progressively rotated to shallower dips (Wernicke, 1995; Collettini, 2011; Abers et al., 1997). Regardless of their geometrical origin, LANFs actively accommodating deformation are now well documented (Webber et al., 2018), including from GNSS measurements (Wallace et al., 2014; Hreinsdóttir and Bennett, 2009; Anderlini et al., 2016; Vadacca et al., 2016; Biemiller et al., 2020a). Some are also clearly delineated by microseismicity (Valoroso et al., 2017; Abers et al., 2016; Rietbrock et al., 1996; Vuan et al., 2020). Moreover, slip rate estimates for 49 active or inactive LANFs (Webber et al., 2018) suggest that these faults slip faster (mostly <10 mm/y but one third >10 mm/y) than their high-angle counterparts (Nicol et al., 2005, mostly <1 mm/y and no faster than 6 mm/y). This observation may be explained by a combination of factors, including a dominant contribution of aseismic slip (Hreinsdóttir and Bennett, 2009). Moreover, due to their shallow dip angle, LANFs are more efficient at accommodating horizontal deformation than regular normal faults, which can result in an apparently higher slip rate when inferred from geodetic data or geological markers of horizontal extension.

Fully dynamic rupture models are physics-based numerical models that couple the non-linear interaction of a fault or fault system's yielding and sliding behavior described by the constitutive laws of friction with seismic wave propagation to simulate the nucleation, propagation, and arrest of a rupture (Andrews, 1976; Day, 1982; Harris et al., 2018; Ramos et al., 2022). Dynamic rupture simulations can be used to understand the initial conditions allowing to reproduce specific aspects of a given earthquake (e.g., Aochi and Madariaga, 2003; Wollherr et al., 2019; Ulrich et al., 2019; Harris et al., 2021; Tinti et al., 2021; Jia et al., 2023b; Hayek et al., 2024), or to understand the influence of specific parameters on rupture characteristics (e.g., Harris et al., 1991; Harris and Day, 1997, 1999; Gabriel et al., 2013; Huang et al., 2014). Recent advances in numerical methods and computational infrastructure have enabled the modeling of increasingly complex problems, in which realistic initial conditions constrained by geological, geophysical, and seismic observations can be included (e.g., 3D multi-segmented fault geometry, fault roughness, spatially variable on- and off-fault initial conditions, topography; Pelties et al., 2012; Heinecke et al., 2014b; Ulrich et al., 2022; Taufiqurrahman et al., 2022, 2023; Jia et al., 2023a; Gabriel et al., 2023). Therefore, dynamic rupture simulations may now be used to forecast realistic rupture scenarios for active fault systems that have not hosted moderate to large earthquakes in modern times. Such scenarios can, in turn, be used to inform seismic hazard assessment by computing associated ground shaking (e.g., Li et al., 2023).

In the Northern Apennines, a LANF, named the Alto Tiberina fault (ATF), accommodates a significant part of the 3 mm/y of extension (Anderlini et al., 2016, Figure 1). Microseismicity, recorded by the dense seismic network of the Alto Tiberina Near fault observatory (TABOO-NFO, Chiaraluce et al., 2014), illuminates the $\sim$17°-dipping low angle normal fault as well as several synthetic and antithetic secondary faults located in its hanging wall (Chiaraluce et al., 2007; Valoroso et al., 2017). Although the ATF is large enough (70 km$\times$40 km) to produce a Mw 7 earthquake, no historical earthquake is known to have occurred on the ATF in the last 1000 years (the completeness limit of the Italian catalog of large historical earthquakes for this part of the Apennines, Boschi, 1998; Castello et al., 2006; Visini et al., 2022).

Here, we used 3D dynamic rupture and seismic wave propagation modeling to forecast plausible scenarios of moderate-to-large earthquakes for the Alto Tiberina low-angle normal fault system, in Italy. We use the multidisciplinary data provided by the TABOO-NFO to help constrain the initial conditions of the simulations. Our dynamic rupture models incorporate multi-segment non-planar fault geometry constrained from seismic data, homogeneous and data-constrained heterogeneous initial stress distributions, slip weakening friction, friction coefficients consistent with the lithology of the area, and topography. In the different models, we investigate the favorable conditions (static fault strength, pre-stress level, nucleation location, fault non-planarity) that enable rupture to propagate. While our simulations show that potential large earthquakes (up to Mw 7.4) are mechanically viable under Andersonian extensional stress conditions for a statically relatively weak ATF (μ_s = 0.37), they also reveal that the non-planarity of the ATF is of primary importance, as dynamic rupture simulations assuming a planar 17°-dipping fault fail to propagate. When the initial stresses are constrained by a coupling model, the rupture remains confined to the coupled parts of the fault, limiting the earthquake magnitude to Mw 6.7. We then discuss the scenarios limitations and potential avenues for future work.

2 The Alto Tiberina Low-Angle Normal Fault

The Alto Tiberina low-angle normal fault (ATF) is located in the inner region of the Umbria-Marche Apennines, Central Italy (Figure 1). It is the easternmost, youngest, and only active fault of six subparallel east-dipping low-angle normal faults that have successively accommodated in the last ∼10 My (along with associated high-angle antithetic normal faults) extension in the Northern Apennines as it migrated eastward (Barchi et al., 1998; Collettini et al., 2002; Collettini and Barchi, 2002). The ATF has accommodated 2 km of slip in the last ∼2 My, leading to a long-term slip rate of 1 mm/y (Collettini and Barchi, 2002). Its main antithetic fault is the Gubbio fault, a N135° striking, 22 km long fault intersecting the ATF at ∼5 km depth (Figure 1). The Gubbio fault has accommodated ∼3 km of slip with a long-term slip rate estimated at 1.65–1.9 mm/y , assuming all the displacement occurred during the Quaternary (Collettini et al., 2003; Mirabella et al., 2004). The present-day regional stress field inferred from focal mechanisms, borehole breakouts, and striated fault planes is characterized by a sub-vertical σ_1 and a subhorizontal, NE-SW trending σ_3 (Lavecchia et al., 1994; Mariucci and Montone, 2014, 2020; Montone and Mariucci, 2016, 2020), suggesting an Andersonian extensional stress-field.

Historical earthquake records report seven historical events, among which three were M>6 earthquakes (in 1352, 1751, and 1781, Figure 1, Rovida et al., 2016). All of them occurred towards the northwestern or southeastern limits of the ATF but none of them is thought to have occurred on the ATF. In instrumental time, three seismic sequences of moderate earthquakes occurred in this area: the 1984 Gubbio (Mw 5.1), the 1997 Colfiorito (Mw 6.0, 5.7 and 5.6) and the 1998 Gualdo Tadino (Mw 5.1) sequences (Figure 1, Haessler et al., 1988; Amato et al., 1998; Chiaraluce et al., 2003; Ciaccio et al., 2006). All main shocks broke NW-trending faults dipping at steep angles (40-50 °) toward the SW. The Gubbio and Gualdo Tadino sequences occurred within the hanging wall of the ATF while the Colfiorito sequence occurred in the SE continuity of the ATF (Figure 1). Note that the Gubbio sequence did not break the Gubbio fault but another steeply-dipping fault segment located between Perugia and Gubbio (Collettini et al., 2003).

Since 2010, the Alto Tiberina fault system is continuously monitored by the Alto Tiberina Near-Fault Observatory TABOO-NFO (Chiaraluce et al., 2014, Figure 1). TABOO-NFO is a multidisciplinary research infrastructure based on state-of-the-art observational systems that monitor in real-time various geophysical parameters to study seismic and aseismic deformation as well as potential preparatory processes on the ATF and nearby faults. In particular, the dense seismic network of TABOO records the seismicity of the Alto Tiberina fault system with a very low event detection threshold (down to M_L=-0.2) and completeness magnitude ($M_C \approx$ 0.5), thus enabling the production of high-resolution earthquake catalogs that finely characterize the architecture of the Alto Tiberina fault system (Chiaraluce et al., 2007; Valoroso et al., 2017; Vuan et al., 2020; Essing and Poli, 2022, 2024; Poggiali et al., 2025).

Microseismicity on the ATF is located between 3 and 16 km depth and defines a 1.5 km thick fault zone (Valoroso et al., 2017; Chiaraluce et al., 2007). The 2010-2014 catalog (Valoroso et al., 2017) reveals that very low magnitude earthquakes ($M_L < 2.4$) occur at a nearly constant rate of 2.2 events per day with a homogeneous spatial distribution, except for one portion located in the northern part of the fault between 7 km and 9 km depth where seismicity is almost absent. In the Alto Tiberina hanging wall, the seismicity rate is 10 times larger and occurs in bursts often associated with Mw>3 mainshock-aftershocks sequences (Valoroso et al., 2017; Vuan et al., 2020, Figure 1) breaking small (few km long) secondary steeply-dipping faults. Such mainshock-aftershocks sequences occurred in the Pietralunga (three Mw 3.2-3.6 events between 2011 and 2014), Città di Castello (five Mw>3 events in 2013), and Gubbio areas (7 Mw>3 events between 2011 and 2014, Figure 1). While the seismicity on the Pietralunga and Città di Castello areas delineates relatively simple structures dipping in only one direction (NE), the seismicity in the Gubbio area is more complex and occurs on oppositely-dipping faults (Valoroso et al., 2017, and Figure 1b). The largest earthquake recorded in the Alto Tiberina hanging wall is a Mw 4.5 earthquake that broke a NE 38° dipping (dip angle from the TDMT solution, https://terremoti.ingv.it/event/34297011) splay of the ATF near the town of Umbertide in 2023 (Figure 1). Finally, no seismicity is associated with the antithetic Gubbio fault.

Modeling of GPS velocities shows that the Alto Tiberina fault system is accommodating two thirds of tectonic extension taking place in the Northern Apennines (Anderlini et al., 2016; Hreinsdóttir and Bennett, 2009; Vadacca et al., 2016) with a geodetic slip rate estimated at 1.7 mm/y on the ATF (Anderlini et al., 2016). Additionally, the distribution of interseismic coupling suggests that a large part of the ATF is creeping but locked near the surface (down to 5 km depth), as well as in the northwestern part of the fault between 7 and 10 km depth (Anderlini et al., 2016, see also Figure 3).

Measurements in boreholes located in the foot-wall of the ATF reveals the presence of CO_2 pressurized at 85% of the lithostatic pressure at around 4 km depth. This over-pressurized fluids are thought to be responsible for the microseismicity on the ATF (Collettini et al., 2002; Collettini and Barchi, 2002; Chiaraluce et al., 2007).

3 Method

We perform 3D dynamic rupture simulations for the Alto Tiberina fault system using *SeisSol*, an open-source software package that solves for spontaneous dynamic rupture and seismic wave propagation with high-order accuracy in space and time (Käser and Dumbser, 2006; Pelties et al., 2014; Heinecke et al., 2014a; Uphoff et al., 2017). SeisSol uses the Arbitrary high-order accurate DERivative Discontinuous Galerkin method (ADER-DG, Dumbser and Käser, 2006) and is optimized for high-performance computing infrastructure. SeisSol uses unstructured tetrahedral meshes allowing representing geometrically complex structures such as non-planar and intersecting faults as well as topography. Dynamic rupture simulations require several initial conditions that need to be prescribed including the fault system geometry (section 3.1), the fault strength (section 3.2), the initial stress state (section 3.3) and the medium properties (section 3.4).

3.1 Fault geometry

Our fault model includes the Alto Tiberina and Gubbio master faults as well as four steeply-dipping secondary faults that have hosted Mw 3.2+ earthquakes since 2010 (Figures 1 and 2). The four secondary faults are the Umbertide, Pietralunga, Gubbio synthetic, and Gubbio antithetic faults. All faults except one are modeled with a realistic non-planar fault geometry. The 3D geometry of the Alto Tiberina and Gubbio master faults is built from the contour depth profiles of Mirabella et al. (2011, 2004), while we use the 2010-2014 seismicity catalog of Valoroso et al. (2017) to constrain the non-planar geometry of three of the secondary faults (Pietralunga, Gubbio synthetic, and Gubbio antithetic faults, supplementary text S1 and Figures S1 and S2). Very recently, Poggiali et al. (2025) have generated another high-resolution catalog covering a longer time span, from 2010 to 2023. This catalog, however, does not modify the first order of geometrical evidence identified by Valoroso et al. (2017). The last secondary fault (Umbertide) is modeled with a planar surface using the focal mechanism of the 2023 Mw 4.5 Umbertide earthquake (https://terremoti.ingv.it/event/34297011).

Our 3D fault geometry generates a heterogeneous dip angle distribution (Figure 2a). While the average dip angle of the Alto Tiberina is 17°, its distribution on the fault is very heterogeneous with values ranging from 4° to 62°. The steepest area is found in the northwestern part of the fault between 6 km and 10 km depth, where a large area exhibits a consistent dip of $\sim$30°. Similarly, the dip angle distribution on the Gubbio fault is highly variable, with a steep dip angle ($\sim$40°) from the surface to 3 km depth and a shallower dip angle, of 18° on average at greater depths. The dip angles of the four secondary faults are steep and range from 38° to 63°.

3.2 Fault Friction

The fault strength evolution during the rupture is described by the widely used linear slip-weakening friction law (Ida, 1972; Palmer et al., 1973; Andrews, 1976; Day, 1982). The fault starts to slip when the initial shear stress τ_o reaches locally the static fault strength $\tau_s = \mu_s \sigma'_n + c$. The fault strength then decreases linearly from its static level τ_s to its dynamic level $\tau_d = \mu_d \sigma'_n$ over a critical slip distance D_c.

The fault core of the low-angle Zuccale fault, the exhumed and inactive analog of the ATF located on the Isle of Elba, is characterized by phyllosilicate-rich rocks (Collettini and Holdsworth, 2004; Collettini et al., 2009). Laboratory friction experiments on samples of the Zuccale phyllosilicate-rich rocks reveal low frictional coefficients (μ_s<0.4, Smith and Faulkner, 2010; Tesei et al., 2012; Niemeijer and Collettini, 2014), with decreasing frictional strength for increasing phyllosilicate content (down to 0.2 for samples with 50$\%$ of phyllosilicate content, Tesei et al., 2012). Consequently, we assume a relatively weak fault with a static friction coefficient μ_s of 0.37 for the reference model.

We set the dynamic friction coefficient μ_d to 0.1 and the critical slip distance D_c to 0.4 m. The frictional cohesion c is set to 0.5 MPa below 3 km depth (up-dip limit of the seismicity on the ATF) and increases linearly up to 1.5 MPa at the surface. The increased frictional cohesion in the first 3 km depth is used here as a proxy to mimic the velocity-strengthening behavior of the shallow part of the crust (Smith and Faulkner, 2010; Niemeijer and Collettini, 2014; Harris et al., 2021; Madden et al., 2022).

3.3 Initial stress

We run two sets of 3D dynamic rupture simulations that assume different initial stress distributions. The first set of simulations assumed laterally uniform Andersonian tectonic loading (section 3.3.1) while the second takes into account stress heterogeneities constrained from the kinematic coupling map of Anderlini et al. (2016) (section 3.3.2).

3.3.1 Uniform initial stress distribution

We consider an Andersonian stress regime for normal-faulting (the maximum compressive stress σ_1 is vertical) with a maximum horizontal compressive stress SHmax (σ_2) oriented 158.8°N (averaged SHmax orientation in the Alto Tiberina area, Mariucci and Montone, 2014, 2020; Montone and Mariucci, 2016). The magnitudes of the principal stresses σ_1, σ_2, and σ_3 ($\sigma_1 > \sigma_2 > \sigma_3$) are controlled by the relative prestress level of a virtual optimally oriented fault R_0, the effective lithostatic stress σ'_z and the stress shape ratio υ (Ulrich et al., 2019). The effective lithostatic stress σ'_z increases linearly with depth and is equal to the lithostatic pressure $\sigma_z = \rho_c g z$ reduced by the effect of the pore fluid pressure P_f. P_f is assumed proportional to the lithostatic stress, $P_f = \gamma \sigma_z$, with γ the fluid-pressure ratio (Ulrich et al., 2019). We assume an average rock density for the crust $\rho_c = 2670$ km/m^3 and an overpressurized state with $\gamma = 0.75$ (consistent with the high fluid pressures measured in the area, Chiaraluce et al., 2007).

Table 1 Parameter values for the homogeneous reference model. Other tested values are listed in brackets.

Stress parameters		
Maximum horizontal stress direction	SH_{max}	158.8°N
Stress-shape ratio	υ	0.5
Pre-stress ratio of an optimally oriented fault	R_0	0.70 [0.65, 0.75]
Fluid pressure ratio	γ	75%
Friction parameters		
Static friction coefficient	μ_s	0.37 [0.30, 0.40, 0.45]
Dynamic friction coefficient	μ_d	0.1
Critical slip weakening distance	D_c	0.4 m
Nucleation parameters		
Nucleation patch radius	r_{nuc}	2.5 km

$$\sigma'_z = (1 - \gamma)\rho g z \tag{1}$$

The stress shape ratio $\upsilon = (\sigma_2 - \sigma_3)/(\sigma_1 - \sigma_3)$ balances the relative magnitudes of the principal stresses (Ulrich et al., 2019) and is set to 0.5 assuming pure normal faulting on an optimally oriented fault. The relative pre-stress level R_0, the ratio of potential stress drop over breakdown strength drop (Aochi and Madariaga, 2003; Ulrich et al., 2019), describes the closeness to failure of a virtual optimally-oriented fault under the Mohr–Coulomb theory. When R_0=1, an optimally oriented fault is critically stressed (Aochi and Madariaga, 2003). R_0 is defined as:

$$R_0 = (\tau_0 - \mu_d \sigma'_n)/((\mu_s - \mu_d)\sigma'_n) \tag{2}$$

Prescribing R_0, μ_s, and μ_d allows for the calculation of the magnitude of the deviatoric stresses. We assume μ_s=0.6 (and μ_d=0.1), therefore, in the assumed stress regime, an optimally oriented fault is a 60°-dipping planar fault (striking in the SHmax direction). We use R_0=0.70 for the reference model and vary this value to evaluate its influence on the scenarios (Table 1 and Figure 4). Since R_0 represents the background pre-stress level relative to fault strength of a virtual, optimally-oriented fault within the assumed stress field, it does not necessarily reflect the ratio of pre-stress level to fault strength on the geometrically complex modeled faults. Therefore, for each tested model, we compute R, the relative pre-stress level resolved on the modeled faults (using the μ_s distribution shown in Figure 2b and μ_d=0.1). Although the faults are loaded with a laterally homogeneous regional stress field (uniform orientation and amplitude of the principal stresses), the normal and shear stresses resolved on the non-planar faults surfaces are spatially variable, leading to heterogeneous values of R (e.g. Figure 4 ans Ulrich et al., 2019). Finally, the deviatoric stresses $(\sigma_1 - \sigma_3)$ are progressively tapered to 0 from 11 to 13 km depth to represent the transition from a brittle to a ductile deformation regime (Boncio et al., 2004). This depth range is consistent with the depth limit of the microseismicity in the Alto Tiberina area (Valoroso et al., 2017). The parameter values used for the reference model, as well as the range of tested values, are shown in Table 1. The result of the homogeneous dynamic rupture simulations are shown in section 4.1

3.3.2 Data-constrained heterogeneous initial stress distribution

The kinematic coupling model (giving the ratio of slip deficit to long-term slip rate) of Anderlini et al. (2016) obtained from interseismic GPS data suggests that while a large part of the ATF is creeping, the fault is mainly coupled near the surface (down to 5 km depth), as well as in the northwestern part of the fault between 7 and 10 km depth. The coupled parts, therefore, accumulate stress while the stress within the creeping parts is continuously released. Here, we use the kinematic coupling model of Anderlini et al. (2016) to constrain the initial stress distribution on the ATF (Ramos et al., 2021; Chan et al., 2023). To that end, we first compute the slip deficit rate SDr using the following equation:

$$SDr = V_o \times IC \tag{3}$$

with V_o the Alto Tiberina long-term slip rate and IC the interseismic kinematic coupling coefficient from Anderlini et al. (2016). We assume $V_o = 1.7$ mm/y (Anderlini et al., 2016). The interseismic coupling coefficient IC ranges between 0 and 1, where 0 means fully creeping fault patches (i.e. slipping at the long-term slip-rate V_o) and 1 means fully coupled fault patches (i.e. not slipping). We use the slip deficit rate as input in a dynamic relaxation simulation with SeisSol (supplementary text S2, Glehman et al., 2024) using the same computational mesh, fault geometries, and material parameters to compute the corresponding stress change rate SCr associated with the slip deficit rate. The slip deficit and shear stress change rates are shown in Figure 3. Following Ramos et al. (2021), we consider a parameter T, defined as the time needed for a certain level of stress to accumulate on the ATF, such as the stress change SC is:

$$SC = SCr \times T \tag{4}$$

The initial stress is then obtained by adding the stress change SC to a background stress state. The background stress state is obtained from the same Andersonian stress field as before (section 3.3.1) but using a pre-stress ratio R_0=0 (supplementary text S2). The static and dynamic coefficients of friction μ_s and μ_d are the same as in the reference homogeneous model. Note that the kinematic coupling model of Anderlini et al. (2016) includes only the ATF. Therefore, in our heterogeneous simulations, only the initial stress distribution on the ATF is constrained by the kinematic coupling model, while the initial stress distribution on the other faults is identical to the homogeneous reference model (with R_0=0.70, section 3.3.1). Therefore, the secondary faults are not affected by the partly-creeping Alto Tiberina fault.

We use T=1800 years, corresponding to the stress accumulation time necessary for the rupture to propagate. We explore T in a range of 1000-3000 years. Values lower than 1600 years do not allow rupture to propagate, while T=1700 years results in a Mw 6.1 earthquake. For values greater than T=2000 years, unrealistic rupture occurs instantaneously across large fault areas. The result of the heterogeneous dynamic rupture simulation is shown in section 4.2.

3.4 Medium properties

We adopt the 1D layered model for the Alto Tiberina area shown in Latorre et al. (2016). This model consists of five crustal layers above the Moho where the shear wave velocity ranges from 2.22 km/s to 3.33 km/s, with a velocity inversion at ∼6 km depth corresponding to Paleozoic-Triassic clastic and metasedimentary rocks (Latorre et al., 2016, and Figure S3). We choose not to use the 3D velocity model of Latorre et al. (2016) due to its limited spatial extent which does not fully cover the ATF and the challenge of merging properly the 3D model with a larger one.

3.5 Nucleation Procedure

The rupture is initiated by linearly decreasing the static frictional strength to the dynamic frictional strength within a gradually expanding nucleation patch of 2.5 km radius (Day et al., 2005; Galis et al., 2015). The nucleation location of our reference model is chosen at ∼8 km depth in an area favorably stressed (Figure 4). Other nucleation locations are also tested on the ATF, at various depths and along-strike positions, as well as on the other faults of the system (Figure 7).

3.6 Computational mesh

Our fault model is included in a structural domain of $500 \times 500 \times 200$ km^3 in the east, north, and vertical direction, respectively. The surface of the domain includes the topography from the SRTM global DEM (Farr et al., 2007) downsampled at 400 m. The structural domain is discretized with tetrahedral elements of variable size using the software *PUMGen* (https://github.com/SeisSol/PUMGen/). *PUMGen* embeds MeshSim from SimMetrix, the underlying mesh generator of SimModeler (www.simmetrix.com), and exports the mesh into the efficient PUML format used by *SeisSol*. The element edge length is 200 m on the faults and gradually coarsened away from the faults. The mesh includes a $110 \times 110 \times 17$ km^3 high-resolution box oriented N140° and covering the Alto Tiberina fault system as well as most stations of the TABOO-NFO (Figure S4). The mesh resolution inside and outside the high-resolution box can resolve frequencies of at least 1 Hz and 0.25 Hz, respectively. However, we note that the use of a 1D velocity model may limit the realism of the simulated ground motions. The mesh comprises 7 million cells.

4 Results

4.1 Homogeneous models

4.1.1 Impact of the pre-stress level

In an Andersonian stress regime for normal faulting, pre-stress levels on an optimally-oriented fault R_0 of 0.75, 0.70 (reference scenario), and 0.65 lead to averaged pre-stress levels R of 0.32, 0.30, and 0.29, respectively, on the ∼17° dipping ATF (Figure 4). Due to the non-planar geometry of the faults, R is very heterogeneous. The northwestern part of the fault below 6 km depth displays several highly pre-stressed patches within which R is 0.8 on average for R_0=0.70. On the contrary, some other parts of the fault are far from failure, such as the northwestern part at shallow depths, that has an average R ratio close to 0. The distribution of R is directly linked to the local dip angle, the shallower is the local dip angle, the lower is the R ratio. This is because, in a stress regime where the maximum compressive stress σ_1 is vertical, areas with shallow dip angle experience larger normal stress and lower shear stress, compared to steeper regions. Similarly, on the Gubbio master fault, highest R values are found at shallow depths, where the mean dip angle is 40° (mean R of 0.28 for R_0=0.70) whereas the deeper part of the Gubbio master fault (mean dip angle of 18°) display lower R values (0.1 on average for R_0=0.70). On the antithetic and synthetic Gubbio faults, as well as on the Pietralunga fault, R values are high (mean of 0.63 for R_0=0.70) due to the steep dip angles of these faults (mean of 53°). Finally, the 38° dipping Umbertide fault has a R of 0.39 for the R_0=0.70 scenario.

R_0 values of 0.75, 0.70, and 0.65 lead to Mw 7.4, Mw 7.3 and Mw 6.9 earthquakes, respectively. Higher pre-stress ratios lead to higher slip amplitudes (averages of 2.2 m, 1.9 m, and 1.4 m, for R_0=0.75, 0.70, and 0.65, respectively) and higher rupture speeds (averages of 1978 km/s, 1709 km/s, and 1258 m/s, Figure 4). Both the R_0=0.75 and R_0=0.70 scenarios break the entire fault (except a small portion at shallow depths in the northwestern part) while the rupture in the R_0=0.65 scenario is confined to the northeastern part of the fault. The rupture of a scenario with R_0=0.60 does not propagate away from the hypocenter (Figure S5). Finally, the Umbertide segment is triggered by the propagating rupture when it reaches the intersection between the ATF and the Umbertide segment. The other segments remain locked (Figure 4a,b).

The moment rate releases of the three scenarios are significantly different, highlighting different rupture behaviors (Figure 6a). The moment rate releases of the R_0=0.75 and reference (R_0=0.70) scenarios both show two main peaks separated by a slower moment rate, but the peak amplitude is lower and the slowdown more pronounced in the reference model. Additionally, despite its larger magnitude, the R_0=0.75 model lasts shorter than the reference model due to its larger rupture speed enabled by its higher pre-stress level (Figure 6a). The R_0=0.65 rupture lasts 40 s. The moment rate is low for the first 15 s before reaching a peak at 22 s.

4.1.2 Impact of the static coefficient of friction μ_s

Figure 5 shows three scenarios where the ATF has a static coefficient of friction μ_s of 0.30, 0.40 and 0.45, respectively (against 0.37 for the reference model shown in Figure 4b). Other parameters are kept unchanged (Table 1). Lower static coefficient of friction μ_s values lead to higher pre-stress levels R on the ATF, resulting in larger earthquake magnitudes and rupture speeds (Figure 5). Static coefficient of friction μ_s values of 0.30, 0.40, and 0.45 lead to moment magnitudes Mw of 7.4, 7.3 and 6.1, respectively. For the latter scenario, the rupture does not propagate far from the nucleation area (Figure 5c).

Interestingly, scenarios having the same moment magnitude and similar final slip distributions do not necessarily have the same dynamics. For example, the R_0=0.75 (μ_s=0.37, Figure 4a) and μ_s=0.30 scenarios (R_0=0.70, Figure 5a) both produce a Mw 7.4 earthquake with a very similar final slip distribution. However, the rupture speed is higher for the μ_s=0.30 scenario (mean rupture speed of 2202 m/s) than for the R_0=0.75 scenario (mean rupture speed of 1978 m/s). This is also shown by their respective moment rate release (Figure 6). The moment rate release of the μ_s=0.30 scenario (Figure 6b) is shorter (30 s) and displays two more pronounced and higher peaks (reaching 1×10^{19} Nm/s) than the R_0=0.75 scenario (Figure 6a, 35 s with highest peak of 0.85×10^{19} Nm/s). Similarly, the reference (μ_s=0.37, R_0=0.7), and μ_s=0.40 (R_0=0.7) scenarios both produce a Mw 7.3 event (Figures 4b and 5b, respectively) but the rupture of the latter lasts 85 s with 3 peaks in the moment rate (reaching $\sim 0.4 \times 10^{19}$ Nm/s, Figure 6b) whereas the rupture of the reference model has a shorter duration (50 s) and a moment rate release with only two peaks reaching a higher amplitude ($\sim 0.6 \times 10^{19}$ Nm/s, Figure 6a).

4.1.3 Influence of the nucleation location

Previous dynamic rupture studies have shown that the nucleation location can significantly impact the rupture extent, slip distribution, and final earthquake size (e.g. Aochi and Ulrich, 2015; Kyriakopoulos et al., 2019; Ramos et al., 2021; Yu et al., 2023; Chan et al., 2023). In this section, we therefore test the impact of the nucleation location on the rupture scenarios. All the initial parameters are identical to those of the reference scenario (Table 1 and Figure 4b), only the nucleation location is changed. We test 13 nucleation locations, 6 on the ATF (Figure 7a), 3 on the master

Gubbio fault (Figure 7b), and one on each of the four other secondary faults (Figure 7c). The nucleation radius on the Alto Tiberina and Gubbio master faults is 2.5 km while we use a nucleation radius of 1.5 km on the smaller secondary faults.

On the ATF, the rupture propagates only when the nucleation is located in a relatively large area of high pre-stress (that is where the local dip angle is steeper, models n°1,6, Figure 7a,d) while the other tested nucleation locations (models n°2-5) fail to propagate. None of the tested nucleation locations on the Gubbio fault leads to a propagating rupture (models n°7-9, Figure 7b,d). Indeed, the relatively shallow dip angle of the Gubbio fault and its high fault strength (μ_s=0.6) do not favor a propagating rupture. Finally, when the nucleation location is located on one of the small secondary segments, the rupture stays confined on the nucleation segment without jumping on the ATF (models n°10-13, Figure 7c,d).

4.2 Data-constrained model

Figure 8 shows the result of the dynamic rupture simulation constrained by the kinematic coupling map of Anderlini et al. (2016). The pre-stress level distribution shows one main high-stressed patch located on the northeastern part of the fault between 4.5 and 9 km depth. Another smaller and less stressed patch is located updip between 1.5 and 3 km depth. These two patches correspond to the areas of greater shear stress change inferred from the kinematic coupling model (Figure 3b). The northeastern part of the fault at shallow depths displays a nearly null pre-stress level (Figure 8a) whereas the same area displays a positive (albeit slight, $\leq$ 2000 Pa/y) slip deficit rate (Figure 3a). This is an indirect impact of the local dip angle, which is very shallow in this area (Figure 2a). This leads to a high normal stress, that in turn, leads to a lower pre-stress ratio. Indeed, the data-constrained model is based on an Andersonian stress regime (see method section 3.3.2). Therefore, the normal stress is modulated by the fault topography, with higher normal stress in areas with shallower dip angles.

The dynamic rupture simulation is nucleated within the highest stressed patch and produces a Mw 6.7 earthquake with 1.3 m of slip on average (maximum of 2.62 m). The rupture is confined within the strongly-coupled patch without propagating upward in the other relatively stressed area (Figure 8b). The rupture last 12 s with an average rupture speed of 1996 m/s (Figures 9 and 8c). A simulation with a nucleation located in the second less stressed patch does not lead to a propagating rupture (Figure S6). We also tested other nucleation locations within the high-stressed patch, as well as lower values of D_c. In each case, the rupture remains confined at depth within the main stressed patch.

4.3 Coulomb stress changes on the hanging wall faults

Our scenarios show that a rupture on the ATF can dynamically trigger the Umbertide fault when the rupture on the main fault reaches the branching intersection (Figures 4, 5). In contrast, in our scenarios, none of the other hanging wall faults is triggered by a rupture on the ATF (Figures 4, 5, and 7). Here we compute the Coulomb stress changes (dCFS) induced by our reference scenario to evaluate the impact of a rupture on the ATF on the closeness to failure of the hanging wall faults (Figure 10). The results show that all secondary faults, except the master Gubbio fault, are brought further away from failure (negative dCFS of $\sim$2 MPa on average, Figure 10c,d,f). The master Gubbio fault is brought closer to failure at depth, near the intersection with the ATF (average positive and maximum dCFS of 1.7 MPa and 9.7 MPa, respectively), but further away from failure above $\sim$3 km depth (-1.1 MPa on average, Figure 10b). Areas of positive dCFS are located where the dip angle is very shallow and thus not well oriented within the Andersonian stress regime. Therefore, under the initial conditions assumed, these positive dCFS do not result in a significantly higher risk of triggering an earthquake, as indicated by the still low pre-stress level R on the Gubbio fault at the end of the simulation (mean R ratio of 0.13 at the end of the simulation, against 0.20 at the beginning, Figure S7).

To obtain a systematic view of the impact of a rupture on the ATF on the hanging wall faults, we compute the Coulomb stress change at different depths for 50°-dipping receiver faults, antithetic and synthetic to the ATF (Figure S8). In the hanging wall of the ATF, the dCFS above 4 km depth and in the immediate vicinity of the ATF (within 10 km of the ATF) is positive (up to 6 MPa). At larger depths and further away from the ATF, the dCFS is negative. We also note positive lobes of dCFS at both along-strike tips of the ATF. These results suggest that a rupture on the ATF would decrease seismic hazard related to the hanging wall faults, except the ones located above 4 km depths near the ATF, whether the receiver faults are synthetic or antithetic to the ATF (Figure S8).

We also compute the peak dynamic Coulomb stress change on the hanging wall faults (Figure S9). The peak dynamic dCFS remain low (<3 MPa) on all secondary faults, except on the Gubbio master fault near the intersection with the ATF, where they reach up to 10 MPa. These dynamic stresses are not high enough to trigger a rupture on the Gubbio master fault during our simulation. Still, it is worth noting that dynamic triggering may be possible if the Gubbio master fault was initially stressed closer to failure, for example, due to different initial conditions such as non-Andersonian stress, higher-pore pressure, or weaker faults.

5 Discussion

5.1 Importance of the ATF geometry and scenario limitations

Our models show that dynamic earthquake rupture can propagate on the ATF only when it nucleates where the local dip angle is $\geq 30°$ (Figures 7 and 2a), suggesting that the geometry of the ATF has a primary impact on where a large earthquake may initiate. To confirm this, we run a simulation having the same initial conditions as our reference scenario but where the ATF is modeled as a 17° dipping planar fault (average dip angle of the ATF). Such fault geometry leads to a uniform R ratio of 0.23 (Figure S10a), too low for the rupture to propagate (Figure S10b). In contrast, when the fault geometry is taken into account, areas of the fault that are more steeply dipping have a R ratio high enough to enable a successful rupture initiation (e.g., Figure 7a). The other parts of the fault do not need to be close to failure to break, the rupture can propagate solely due to the large dynamic stresses arising from the rupture front.

Uncertainties of the ATF geometry may impact our results. We use the fault geometry estimated by Mirabella et al. (2011) from 40 seismic reflection profiles and six boreholes. The seismic reflection profiles are unevenly distributed, suggesting that some areas of the fault are less well constrained than others (see Figure 13 in Mirabella et al., 2011). One way to increase the precision of the fault geometry would be to use the TABOO-NFO microseismicity catalog to verify and adjust the geometry of the ATF in areas not covered by the seismic reflection profiles (e.g., Palgunadi et al., 2020). Another source of uncertainty stems from the initial stress distribution. For example, we here do not take into account potential remnant stress changes due to the previous large earthquakes in the area. Our initial stress distribution of the heterogeneous scenario is constrained by a kinematic coupling map estimated from unevenly distributed GPS data. In particular, the southeast half of the fault is not well covered by GPS stations, and coupled portions of the fault could be missed by the current GPS network (Anderlini et al., 2016). Moreover, both the magnitude and spatial distribution of stress on secondary faults, such as those near Gubbio, Umbertide and Pietralunga remain poorly constrained. Higher stress amplitudes or different stress distributions could potentially facilitate rupture on these faults. In this study, we explore a range of plausible rupture scenarios, but we acknowledge that assuming different frictional and elastic properties or a different stress accumulation pattern could lead to significantly different rupture behaviors. For instance, incorporating 3D variations in elastic properties could affect the dynamic triggering potential of the hanging wall faults. Finally, our choice of friction law and parametrization may underestimate the dynamic triggering potential compared to rapid velocity-weakening and restrengthening rate-and-state friction behavior (Gabriel et al., 2024).

5.2 Low angle normal fault mechanics

Various explanations have been proposed to explain the mechanical paradox of LANFs. Some propose that the stress field around LANFs could be non-Andersonian and oriented in such a way that favors slip on a LANF (e.g. Abers et al., 1997; Westaway, 1999; Lister and Davis, 1989; Wernicke, 1995; Yin, 1989, 1991; Melosh, 1990; Spencer and Chase, 1989). Alternatively, high fluid pressures could facilitate slip by reducing the effective normal stress (e.g. Axen, 1992; Collettini and Barchi, 2002). Finally, fault rocks of LANFs could be statically or dynamically weak (Townend and Zoback, 2001; Lavier and Buck, 2002; Collettini, 2011; Collettini et al., 2019; Lavier et al., 1999; Biemiller et al., 2022, 2023).

In this paper, we show that a large rupture on a LANF under a perfectly Andersonian stress regime is mechanically viable. This is consistent with Biemiller et al. (2022) that present dynamic rupture simulations for the Mai'iu, Papua New Guinea, LANF. Their models assume a rate-and-state with strong velocity weakening friction law with an estimated equivalent static friction coefficient $\mu_s \approx f_0 = 0.6$ and a critically stressed fault. Here, the fault does not need to be critically stressed to rupture (R_0=0.70 in our preferred model against R_0=0.95 in Biemiller et al., 2022). Instead, it is the low static coefficient of friction on the Alto Tiberina fault (μ_s=0.37 in our reference model) along with a nucleation on the steeper part of the fault that allows a successful rupture propagation.

In our scenarios, 60° dipping faults with a static friction coefficient of μ_s=0.6 would be optimally oriented in the Andersonian normal faulting regime we assume. Steeply-dipping normal faults in the hanging wall are therefore expected to reach failure before the on average 17° dipping ATF. This is not the case in our scenarios, best-oriented (i.e steeper) parts of the ATF have a pre-stress ratio R similar or higher to the steep hanging wall faults due to the smaller ATF static coefficient of friction.

The heterogeneous scenario, geodetically-constrained from the coupling map of Anderlini et al. (2016), leads to a Mw 6.7 rupture confined in the coupled asperity at depth (Figure 8). The rupture is not able to propagate within the other asperity located at shallower depth due to a narrow zone where both the lower coupling coefficient and the fault geometry lead to a very low pre-stress level that acts as a barrier to the rupture propagation, nor within the creeping zones (Figures 3 and 8). Since this scenario is constrained by data, it can be considered more likely to occur than the homogeneous reference scenario, which breaks the entire fault and results in a significantly larger earthquake (Mw 7.3). However, it is important to note that our models do not incorporate fast velocity weakening rate-and-state friction (Ampuero and Ben-Zion, 2008; Noda et al., 2009) observed in laboratory experiments (e.g. Di Toro et al., 2011;

Kohli et al., 2011) and thought to account for physical weakening processes operating on natural faults at the high slip velocities typical of dynamic earthquake rupture (Rice, 2006).Incorporating such a frictional law facilitates the concept of statically strong and dynamically weak faults, and enables a range of rupture complexities and fault interactions (Dunham et al., 2011; Taufiqurrahman et al., 2023; Palgunadi et al., 2024). For example, in dynamic rupture simulations for the Mai'iu low angle normal fault, velocity-weakening friction law allowed rupture to propagate into a shallow velocity-strengthening portion of the fault (Biemiller et al., 2022). Similarly, fully dynamic seismic cycle simulations with rate-and-state friction laws show that ruptures can propagate through velocity-strengthening barriers under specific conditions (Kaneko et al., 2010). Additionally such friction laws allow faults to rupture at relatively low shear stress levels (e.g. Ulrich et al., 2019). Incorporating a strong velocity weakening friction law in simulations for the ATF would therefore be highly relevant. While this is beyond the scope of the present study, we consider this an important direction for future work.

5.3 Realistic rupture scenarios for seismic hazard assessment and rapid response

Due to the scarcity of large LANF earthquakes, seismic hazard associated with these structures is poorly constrained. By identifying a number of potential rupture scenarios, 3D dynamic rupture simulations can help constraining seismic hazard in such regions where the instrumental record lacks large earthquakes (Ramos et al., 2021; Biemiller et al., 2022; Li et al., 2023). To produce scenarios as realistic and precise as possible, geophysical and geological observations must be integrated to constrain the initial conditions of the simulations (e.g. Ramos and Huang, 2019; Ramos et al., 2021; Biemiller et al., 2022; Li et al., 2023). For instance, as in our study, seismic data such as seismic reflection profiles and high-resolution seismicity catalogs can be used to constrain the often complex geometry of a fault system. Analyses of exposed fault surfaces can help constrain small-scale geometrical complexities (fault roughness, e.g. Power et al., 1987; Candela et al., 2010), which can then be integrated in dynamic rupture models (e.g. Bruhat et al., 2020; Taufiqurrahman et al., 2022). Additionally, seismic, geodetic, and field analyses can also constrain the shape and characteristics of damages zones (e.g. Li et al., 2007; Mitchell and Faulkner, 2009; Rodriguez Padilla et al., 2022), while laboratory experiments made on fault zone rocks can help determined frictional properties of faults. Those data-informed physic-based scenarios can then be used to simulate realistic ground motions (e.g. Taufiqurrahman et al., 2022; Li et al., 2023) and to compute shake maps (Figure S11).

Dynamic rupture scenarios can also be used in rapid-response workflows for rapid source and associated shakemaps determination. Contrary to rapid data-driven kinematic source characterization workflows (e.g. Hayes, 2017; Goldberg et al., 2022; Delouis, 2014) that provide results within hours after an earthquake, complex dynamic rupture simulations such as the ones presented in this paper are more computationally expensive (90 s of simulation requires $\sim$3000 CPU hours) and require super-computing facilities. To overcome this limitation, a catalog of rupture scenarios for a given fault system can be produced in advance and compared with early observations (e.g., seismic waveforms, moment-rate release) when an earthquake happens. The best-fitting scenario(s) of the catalog would provide a first-order but physically consistent representation of the event and the associated shake maps could help emergency responses. Such rapid-response dynamic source determination workflow based on a pre-built catalog of realistic physic-based scenarios is currently under development within the DT-GEO project (https://dtgeo.eu/) for the Alto Tiberina fault system, which is integrated into this project as a site demonstrator (Figure S12).

Finally, such a catalog of scenarios can also be the base of machine-learning training. For example, after training a Reduced-Order Model (ROM) using the scenarios of the pre-built catalog, the ROM can be evaluated for any point of the parameter space defined by the training catalog (e.g. Rekoske et al., 2023). The advantage is that ROMs are computationally cheap models that can enable the evaluation of new earthquake scenarios instantaneously (in milliseconds) without resorting to HPC infrastructures.

6 Conclusion

In this study, we show that large earthquakes (up to Mw 7.4) on the 17°-dipping Alto Tiberina low-angle normal fault (ATF) are mechanically viable under Andersonian extensional stress conditions, and assuming a statically relatively weak fault (μ_s = 0.37). We show that local heterogeneities in the geometry of the ATF, which result in a non-planar fault surface, are of critical importance, as dynamic ruptures can nucleate only at favorably oriented, steeper parts of the faults ($\geq\sim30°$ dip). When initial conditions are constrained by a geodetic coupling map, dynamic ruptures remain confined to the coupled part of the Alto Tiberina fault, limiting earthquake magnitudes to Mw 6.7. These results suggest that detailed knowledge of fault geometry and kinematic coupling distribution provides valuable insights into where large ruptures can nucleate and propagate on low-angle normal faults. In our simulations, earthquakes nucleating on secondary faults cannot propagate onto the ATF. However, ruptures on the ATF can dynamically trigger a small synthetic branch connected to the ATF but not the more distant, disconnected secondary faults. Coulomb stress change analysis shows that an ATF rupture may reduce seismic hazard related to the hanging wall faults, except for those located above 4 km depth near the ATF. Finally, we argue that data-informed 3D dynamic rupture simulations are key to advancing accurate earthquake rupture forecasting and physics-based seismic hazard assessment. Pre-built catalogs of dynamic rupture scenarios can be integrated into rapid-response workflows, enabling rapid source characterization and associated shake-map generation.

Data and code availability

The dynamic rupture simulations were performed using SeisSol (www.seissol.org), an open-source software freely available to download from https://github.com/SeisSol/SeisSol/. We use SeisSol, commit 01ae1b1. All data required to reproduce the dynamic rupture scenarios (i.e. computational mesh and SeisSol input files) can be downloaded from the Zenodo repository 10.5281/zenodo.14895123. Instructions for downloading, installing, and running the code are available in the SeisSol documentation at https://seissol.readthedocs.io/. Downloading and compiling instructions are at https://seissol.readthedocs.io/en/latest/compiling-seissol.html. Instructions for setting up and running simulations are at https://seissol.readthedocs.io/en/latest/configuration.html. Quickstart containerized installations and introductory materials are provided in the docker container and jupyter notebooks at https://github.com/SeisSol/Training. Example problems and model configuration files are provided at https://github.com/SeisSol/Examples, many of which reproduce the SCEC 3D Dynamic Rupture benchmark problems described at https://strike.scec.org/cvws/benchmark_descriptions.html.

Competing interests

The authors declare no competing interests.

Acknowledgments

We thank the Handling Editor Marlon Ramos, an anonymous reviewer, and the internal USGS reviewer Ruth Harris for their thoughtful and constructive comments. This study was supported by Horizon Europe (DT-GEO, grant number 101058129, Geo-INQUIRE, grant number 101058518 and ChEESE-2P, grant number 101093038). AAG acknowledges additional support from the National Science Foundation (NSF grant numbers EAR-2225286, EAR-2121568, OAC-2139536, OAC-2311208) and the National Aeronautics and Space Administration (NASA 80NSSC20K0495). We thank the Gauss Centre for Supercomputing e.V. (www.gauss-centre.eu) for providing us with computing time on the supercomputer SuperMUC-NG at the Leibniz Supercomputing Centre (www.lrz.de) in project pn49ha. Additional computing resources were provided by the Institute of Geophysics of LMU Munich (Oeser et al., 2006). Any use of trade, firm, or product names is for descriptive purposes only and does not imply endorsement by the U.S. Government.

References

Abers, G., Eilon, Z., Gaherty, J., Jin, G., Kim, Y., Obrebski, M., and Dieck, C. Southeast Papuan crustal tectonics: Imaging extension and buoyancy of an active rift. *Journal of Geophysical Research: Solid Earth*, 121(2):951–971, 2016.

Abers, G. A. Possible seismogenic shallow-dipping normal faults in the Woodlark-D'Entrecasteaux extensional province, Papua New Guinea. *Geology*, 19(12):1205–1208, 1991.

Abers, G. A., Mutter, C. Z., and Fang, J. Shallow dips of normal faults during rapid extension: Earthquakes in the Woodlark-D'Entrecasteaux rift system, Papua New Guinea. *Journal of Geophysical Research: Solid Earth*, 102(B7):15301–15317, 1997.

Amato, A., Azzara, R., Chiarabba, C., Cimini, G., Cocco, M., Di Bona, M., Margheriti, L., Mazza, S., Mele, F., Selvaggi, G., et al. The 1997 Umbria-Marche, Italy, earthquake sequence: A first look at the main shocks and aftershocks. *Geophysical Research Letters*, 25(15):2861–2864, 1998.

Ampuero, J.-P. and Ben-Zion, Y. Cracks, pulses and macroscopic asymmetry of dynamic rupture on a bimaterial interface with velocity-weakening friction. *Geophysical Journal International*, 173(2):674–692, 2008.

Anderlini, L., Serpelloni, E., and Belardinelli, M. E. Creep and locking of a low-angle normal fault: Insights from the Altotiberina fault in the northern Apennines (Italy). *Geophysical Research Letters*, 43(9):4321–4329, 2016.

Anderson, E. M. The dynamics of faulting. *Transactions of the Edinburgh Geological Society*, 8(3):387–402, 1905.

Anderson, E. M. The dynamics of faulting and dyke formation with applications to Britain. *(No Title)*, 1951.

Andrews, D. Rupture propagation with finite stress in antiplane strain. *Journal of Geophysical Research*, 81(20):3575–3582, 1976.

Aochi, H. and Madariaga, R. The 1999 Izmit, Turkey, earthquake: Nonplanar fault structure, dynamic rupture process, and strong ground motion. *Bulletin of the Seismological Society of America*, 93(3):1249–1266, 2003.

Aochi, H. and Ulrich, T. A probable earthquake scenario near Istanbul determined from dynamic simulations. *Bulletin of the Seismological Society of America*, 105(3):1468–1475, 2015.

Axen, G. J. Pore pressure, stress increase, and fault weakening in low-angle normal faulting. *Journal of Geophysical Research: Solid Earth*, 97(B6):8979–8991, 1992.

Axen, G. J. Mechanics of low-angle normal faults. In *Rheology and deformation of the lithosphere at continental margins*, pages 46–91. Columbia University Press, 2004.

Barchi, M., De Feyter, A., Magnani, M., Minelli, G., Pialli, G., and Sotera, B. Extensional tectonics in the Northern Apennines (Italy): evidence from the CROP03 deep seismic reflection line. *Mem. Soc. Geol. It*, 52:527–538, 1998.

Biemiller, J., Boulton, C., Wallace, L., Ellis, S., Little, T., Mizera, M., Niemeijer, A., and Lavier, L. Mechanical implications of creep and partial coupling on the world's fastest slipping low-angle normal fault in southeastern Papua New Guinea. *Journal of Geophysical Research: Solid Earth*, 125(10):e2020JB020117, 2020a.

Biemiller, J., Taylor, F., Lavier, L., Yu, T.-L., Wallace, L., and Shen, C.-C. Emerged coral reefs record Holocene low-angle normal fault earthquakes. *Geophysical Research Letters*, 47(20):e2020GL089301, 2020b.

Biemiller, J., Gabriel, A.-A., and Ulrich, T. The dynamics of unlikely slip: 3D modeling of low-angle normal fault rupture at the Mai'iu fault, Papua New Guinea. *Geochemistry, Geophysics, Geosystems*, 23(5):e2021GC010298, 2022.

Biemiller, J., Gabriel, A.-A., and Ulrich, T. Dueling dynamics of low-angle normal fault rupture with splay faulting and off-fault damage. *Nature Communications*, 14(1):2352, 2023.

Boncio, P., Lavecchia, G., and Pace, B. Defining a model of 3D seismogenic sources for Seismic Hazard Assessment applications: The case of central Apennines (Italy). *Journal of Seismology*, 8:407–425, 2004.

Boschi, E. *I terremoti dell'Appennino umbro-marchigiano: area sud orientale dal 99 aC al 1984*. Editrice Compositori, 1998.

Bruhat, L., Klinger, Y., Vallage, A., and Dunham, E. M. Influence of fault roughness on surface displacement: From numerical simulations to coseismic slip distributions. *Geophysical Journal International*, 220(3):1857–1877, 2020.

Candela, T., Renard, F., Bouchon, M., Brouste, A., Marsan, D., Schmittbuhl, J., and Voisin, C. Characterization of fault roughness at various scales: Implications of three-dimensional high resolution topography measurements. *Mechanics, structure and evolution of fault zones*, pages 1817–1851, 2010.

Castello, B., Selvaggi, G., Chiarabba, C., and Amato, A. CSI Catalogo della sismicità italiana 1981-2002, versione 1.1. INGV-CNT, Roma, 2006.

Chan, Y. P. B., Yao, S., and Yang, H. Impact of hypocenter location on rupture extent and ground motion: A case study of southern cascadia. *Journal of Geophysical Research: Solid Earth*, 128(8):e2023JB026371, 2023.

Chiaraluce, L., Ellsworth, W., Chiarabba, C., and Cocco, M. Imaging the complexity of an active normal fault system: The 1997 Colfiorito (central Italy) case study. *Journal of Geophysical Research: Solid Earth*, 108(B6), 2003.

Chiaraluce, L., Chiarabba, C., Collettini, C., Piccinini, D., and Cocco, M. Architecture and mechanics of an active low-angle normal fault: Alto Tiberina fault, northern Apennines, Italy. *Journal of Geophysical Research: Solid Earth*, 112(B10), 2007.

Chiaraluce, L., Amato, A., Carannante, S., Castelli, V., Cattaneo, M., Cocco, M., Collettini, C., D'Alema, E., Di Stefano, R., Latorre, D., et al. The alto Tiberina near fault observatory (northern Apennines, Italy). *Annals of Geophysics*, 2014.

Ciaccio, M. G., Pondrelli, S., and Frepoli, A. Earthquake fault-plane solutions and patterns of seismicity within the Umbria Region, Italy. 2006.

Collettini, C. The mechanical paradox of low-angle normal faults: Current understanding and open questions. *Tectonophysics*, 510(3-4): 253–268, 2011.

Collettini, C. and Barchi, M. R. A low-angle normal fault in the Umbria region (Central Italy): a mechanical model for the related microseismicity. *Tectonophysics*, 359(1-2):97–115, 2002.

Collettini, C. and Holdsworth, R. Fault zone weakening and character of slip along low-angle normal faults: insights from the Zuccale fault, Elba, Italy. *Journal of the Geological Society*, 161(6):1039–1051, 2004.

Collettini, C. and Sibson, R. H. Normal faults, normal friction? *Geology*, 29(10):927–930, 2001.

Collettini, C., Barchi, M. R., Chiaraluce, L., Mirabella, F., and Pucci, S. The Gubbio fault: can different methods give pictures of the same object? *Journal of Geodynamics*, 36(1-2):51–66, 2003.

Collettini, C., Viti, C., Smith, S. A., and Holdsworth, R. E. Development of interconnected talc networks and weakening of continental low-angle normal faults. *Geology*, 37(6):567–570, 2009.

Collettini, C., Tesei, T., Scuderi, M. M., Carpenter, B. M., and Viti, C. Beyond Byerlee friction, weak faults and implications for slip behavior. *Earth and Planetary Science Letters*, 519:245–263, 2019.

Collettini, C. et al. Hypothesis for the mechanics and seismic behaviour of low-angle normal faults: the example of the Altotiberina fault Northern Apennines. *Annals of Geophysics*, 2002.

Cummins, P. R., Pranantyo, I. R., Pownall, J. M., Griffin, J. D., Meilano, I., and Zhao, S. Earthquakes and tsunamis caused by low-angle normal faulting in the Banda Sea, Indonesia. *Nature Geoscience*, 13(4):312–318, 2020.

Day, S. M. Three-dimensional simulation of spontaneous rupture: The effect of nonuniform prestress. *Bulletin of the Seismological Society of America*, 72(6A):1881–1902, Dec. 1982. doi: 10.1785/BSSA07206A1881.

Day, S. M., Dalguer, L. A., Lapusta, N., and Liu, Y. Comparison of finite difference and boundary integral solutions to three-dimensional spontaneous rupture. *Journal of Geophysical Research: Solid Earth*, 110(B12), 2005.

Delouis, B. FMNEAR: Determination of focal mechanism and first estimate of rupture directivity using near-source records and a linear distribution of point sources. *Bulletin of the Seismological Society of America*, 104(3):1479–1500, 2014.

Di Toro, G., Han, R., Hirose, T., De Paola, N., Nielsen, S., Mizoguchi, K., Ferri, F., Cocco, M., and Shimamoto, T. Fault lubrication during earthquakes. *Nature*, 471(7339):494–498, 2011.

Dumbser, M. and Käser, M. An arbitrary high-order discontinuous Galerkin method for elastic waves on unstructured meshes—II. The three-dimensional isotropic case. *Geophysical Journal International*, 167(1):319–336, 2006.

Dunham, E. M., Belanger, D., Cong, L., and Kozdon, J. E. Earthquake ruptures with strongly rate-weakening friction and off-fault plasticity, Part 1: Planar faults. *Bulletin of the Seismological Society of America*, 101(5):2296–2307, 2011.

Essing, D. and Poli, P. Spatiotemporal evolution of the seismicity in the alto tiberina fault system revealed by a high-resolution template matching catalog. *Journal of Geophysical Research: Solid Earth*, 127(10):e2022JB024845, 2022.

Essing, D. and Poli, P. Unraveling earthquake clusters composing the 2014 Alto Tiberina earthquake swarm via unsupervised learning. *Journal of Geophysical Research: Solid Earth*, 129(1):e2022JB026237, 2024.

Farr, T. G., Rosen, P. A., Caro, E., Crippen, R., Duren, R., Hensley, S., Kobrick, M., Paller, M., Rodriguez, E., Roth, L., et al. The shuttle radar topography mission. *Reviews of geophysics*, 45(2), 2007.

Gabriel, A.-A., Ampuero, J.-P., Dalguer, L., and Mai, P. M. Source properties of dynamic rupture pulses with off-fault plasticity. *Journal of Geophysical Research: Solid Earth*, 118(8):4117–4126, 2013.

Gabriel, A.-A., Ulrich, T., Marchandon, M., Biemiller, J., and Rekoske, J. 3D Dynamic Rupture Modeling of the 6 February 2023, Kahramanmaraş, Turkey M w 7.8 and 7.7 Earthquake Doublet Using Early Observations. *The Seismic Record*, 3(4):342–356, 2023.

Gabriel, A.-A., Garagash, D. I., Palgunadi, K. H., and Mai, P. M. Fault size–dependent fracture energy explains multiscale seismicity and cascading earthquakes. *Science*, 385(6707):eadj9587, 2024.

Galis, M., Pelties, C., Kristek, J., Moczo, P., Ampuero, J.-P., and Mai, P. M. On the initiation of sustained slip-weakening ruptures by localized stresses. *Geophysical Journal International*, 200(2):890–909, 2015.

Glehman, J., Gabriel, A.-A., Ulrich, T., Ramos, M. D., Huang, Y., and Lindsey, E. O. Partial ruptures governed by the complex interplay between geodetic slip deficit, rigidity, and pore fluid pressure in 3D Cascadia dynamic rupture simulations. 2024.

Goldberg, D. E., Koch, P., Melgar, D., Riquelme, S., and Yeck, W. L. Beyond the teleseism: Introducing regional seismic and geodetic data into routine USGS finite-fault modeling. *Seismological Society of America*, 93(6):3308–3323, 2022.

Haessler, H., Gaulon, R., Rivera, L., Console, R., Frogneux, M., Gasparini, G., Martel, L., Patau, G., Siciliano, M., and Cisternas, A. The Perugia (Italy) earthquake of 29, April 1984: a microearthquake survey. *Bulletin of the Seismological Society of America*, 78(6):1948–1964, 1988.

Harris, R. A. and Day, S. M. Effects of a low-velocity zone on a dynamic rupture. *Bulletin of the Seismological Society of America*, 87(5): 1267–1280, 1997.

Harris, R. A. and Day, S. M. Dynamic 3D simulations of earthquakes on en echelon faults. *Geophysical Research Letters*, 26(14):2089–2092, 1999.

Harris, R. A., Archuleta, R. J., and Day, M. Fault steps and the dynamic rupture process: 2-D numerical simulations of a spontaneously propagating shear fracture. *Geophysical Research Letters*, 18:893–896, 1991.

Harris, R. A., Barall, M., Aagaard, B., Ma, S., Roten, D., Olsen, K., Duan, B., Liu, D., Luo, B., Bai, K., et al. A suite of exercises for verifying dynamic earthquake rupture codes. *Seismological Research Letters*, 89(3):1146–1162, 2018.

Harris, R. A., Barall, M., Lockner, D. A., Moore, D. E., Ponce, D. A., Graymer, R., Funning, G., Morrow, C. A., Kyriakopoulos, C., and Eberhart-Phillips, D. A geology and geodesy based model of dynamic earthquake rupture on the Rodgers Creek-Hayward-Calaveras fault system, California. *Journal of Geophysical Research: Solid Earth*, 126(3):e2020JB020577, 2021.

Hayek, J. N., Marchandon, M., Li, D., Pousse-Beltran, L., Hollingsworth, J., Li, T., and Gabriel, A.-A. Non-Typical Supershear Rupture: Fault Heterogeneity and Segmentation Govern Unilateral Supershear and Cascading Multi-Fault Rupture in the 2021 7.4 Maduo Earthquake. *Geophysical Research Letters*, 51(20):e2024GL110128, 2024. doi: https://doi.org/10.1029/2024GL110128.

Hayes, G. P. The finite, kinematic rupture properties of great-sized earthquakes since 1990. *Earth and Planetary Science Letters*, 468:94–100, 2017.

Heinecke, A., Breuer, A., Rettenberger, S., Bader, M., Gabriel, A.-A., Pelties, C., Bode, A., Barth, W., Liao, X.-K., Vaidyanathan, K., Smelyanskiy, M., and Dubey, P. Petascale High Order Dynamic Rupture Earthquake Simulations on Heterogeneous Supercomputers. In *SC '14: Proceedings of the International Conference for High Performance Computing, Networking, Storage and Analysis*, pages 3–14, 2014a. doi: 10.1109/SC.2014.6.

Heinecke, A., Breuer, A., Rettenberger, S., Bader, M., Gabriel, A.-A., Pelties, C., Bode, A., Barth, W., Liao, X.-K., Vaidyanathan, K., et al. Petascale high order dynamic rupture earthquake simulations on heterogeneous supercomputers. In *SC'14: Proceedings of the International Conference for High Performance Computing, Networking, Storage and Analysis*, pages 3–14. IEEE, 2014b.

Hreinsdóttir, S. and Bennett, R. A. Active aseismic creep on the Alto Tiberina low-angle normal fault, Italy. *Geology*, 37(8):683–686, 2009.

Huang, Y., Ampuero, J.-P., and Helmberger, D. V. Earthquake ruptures modulated by waves in damaged fault zones. *Journal of Geophysical Research: Solid Earth*, 119(4):3133–3154, 2014.

Ida, Y. Cohesive force across the tip of a longitudinal-shear crack and Griffith's specific surface energy. *Journal of Geophysical Research (1896-1977)*, 77(20):3796–3805, 1972. doi: 10.1029/JB077i020p03796.

Jia, Z., Jin, Z., Marchandon, M., Ulrich, T., Gabriel, A.-A., Fan, W., Shearer, P., Zou, X., Rekoske, J., Bulut, F., Garagon, A., and Fialko, Y. The complex dynamics of the 2023 Kahramanmaraş, Turkey, Mw 7.8-7.7 earthquake doublet. *Science*, 0:eadi0685, 2023a. doi: 10.1126/science.adi0685.

Jia, Z., Jin, Z., Marchandon, M., Ulrich, T., Gabriel, A.-A., Fan, W., Shearer, P., Zou, X., Rekoske, J., Bulut, F., et al. The complex dynamics of the 2023 Kahramanmaraş, Turkey, M w 7.8-7.7 earthquake doublet. *Science*, 381(6661):985–990, 2023b.

Kaneko, Y., Avouac, J.-P., and Lapusta, N. Towards inferring earthquake patterns from geodetic observations of interseismic coupling. *Nature Geoscience*, 3(5):363–369, 2010.

Karlsson, K. W., Rockwell, T. K., Fletcher, J. M., Figueiredo, P. M., Rosas, J. F. C., Gontz, A. M., Naik, S. P., Lacan, P., Spelz, R. M., Owen, L. A., et al. Large Holocene ruptures on the Cañada David detachment, Baja California, Mexico; implications for the seismogenesis of low-angle normal faults. *Earth and Planetary Science Letters*, 570:117070, 2021.

Kohli, A. H., Goldsby, D. L., Hirth, G., and Tullis, T. Flash weakening of serpentinite at near-seismic slip rates. *Journal of Geophysical Research: Solid Earth*, 116(B3), 2011.

Kyriakopoulos, C., Oglesby, D., Rockwell, T., Meltzner, A., Barall, M., Fletcher, J. M., and Tulanowski, D. Dynamic rupture scenarios in the Brawley seismic zone, Salton Trough, Southern California. *Journal of Geophysical Research: Solid Earth*, 124(4):3680–3707, 2019.

Käser, M. and Dumbser, M. An arbitrary high-order discontinuous Galerkin method for elastic waves on unstructured meshes — I. The two-dimensional isotropic case with external source terms. *Geophysical Journal International*, 166(2):855–877, 08 2006. doi: 10.1111/j.1365-246X.2006.03051.x.

Latorre, D., Mirabella, F., Chiaraluce, L., Trippetta, F., and Lomax, A. Assessment of earthquake locations in 3-D deterministic velocity models: A case study from the Altotiberina Near Fault Observatory (Italy). *Journal of Geophysical Research: Solid Earth*, 121(11):8113–8135, 2016.

Lavecchia, G., Brozzetti, F., Barchi, M., Menichetti, M., and Keller, J. V. Seismotectonic zoning in east-central Italy deduced from an analysis of the Neogene to present deformations and related stress fields. *Geological Society of America Bulletin*, 106(9):1107–1120, 1994.

Lavier, L. L. and Buck, W. R. Half graben versus large-offset low-angle normal fault: Importance of keeping cool during normal faulting. *Journal of Geophysical Research: Solid Earth*, 107(B6):ETG–8, 2002.

Lavier, L. L., Roger Buck, W., and Poliakov, A. N. Self-consistent rolling-hinge model for the evolution of large-offset low-angle normal faults. *Geology*, 27(12):1127–1130, 1999.

Li, B., Gabriel, A.-A., Ulrich, T., Abril, C., and Halldorsson, B. Dynamic rupture models, fault interaction and ground motion simulations for the segmented Húsavík-Flatey Fault Zone, Northern Iceland. *Journal of Geophysical Research: Solid Earth*, 128(6):e2022JB025886, 2023.

Li, H., Zhu, L., and Yang, H. High-resolution structures of the Landers fault zone inferred from aftershock waveform data. *Geophysical Journal International*, 171(3):1295–1307, 2007.

Lister, G. S. and Davis, G. A. The origin of metamorphic core complexes and detachment faults formed during Tertiary continental extension in the northern Colorado River region, USA. *Journal of Structural Geology*, 11(1-2):65–94, 1989.

Little, T. A., Webber, S., Mizera, M., Boulton, C., Oesterle, J., Ellis, S., Boles, A., Van der Pluijm, B., Norton, K., Seward, D., et al. Evolution of a rapidly slipping, active low-angle normal fault, Suckling-Dayman metamorphic core complex, SE Papua New Guinea. *GSA Bulletin*, 131 (7-8):1333–1363, 2019.

Madden, E. H., Ulrich, T., and Gabriel, A.-A. The state of pore fluid pressure and 3-D megathrust earthquake dynamics. *Journal of Geophysical Research: Solid Earth*, 127(4):e2021JB023382, 2022.

Mariucci, M. T. and Montone, P. Database of Italian Present-day Stress Indicators, Istituto Nazionale di Geofisica e Vulcanologia (INGV), 2014. doi: 10.13127/IPSI.1.6.

Mariucci, M. T. and Montone, P. Database of Italian present-day stress indicators, IPSI 1.4. *Scientific data*, 7(1):298, 2020.

Melosh, H. Mechanical basis for low-angle normal faulting in the Basin and Range province. *Nature*, 343(6256):331–335, 1990.

Mirabella, F., Ciaccio, M., Barchi, M. R., and Merlini, S. The Gubbio normal fault (Central Italy): geometry, displacement distribution and tectonic evolution. *Journal of Structural Geology*, 26(12):2233–2249, 2004.

Mirabella, F., Brozzetti, F., Lupattelli, A., and Barchi, M. R. Tectonic evolution of a low-angle extensional fault system from restored cross-sections in the Northern Apennines (Italy). *Tectonics*, 30(6), 2011.

Mitchell, T. and Faulkner, D. The nature and origin of off-fault damage surrounding strike-slip fault zones with a wide range of displacements: A field study from the Atacama fault system, northern Chile. *Journal of Structural Geology*, 31(8):802–816, 2009.

Mizera, M., Little, T., Biemiller, J., Ellis, S., Webber, S., and Norton, K. Structural and geomorphic evidence for rolling-hinge style deformation of an active continental low-angle normal fault, SE Papua New Guinea. *Tectonics*, 38(5):1556–1583, 2019.

Montone, P. and Mariucci, M. T. The new release of the Italian contemporary stress map. *Geophysical Journal International*, 205(3):1525–1531, 2016.

Montone, P. and Mariucci, M. T. Constraints on the structure of the shallow crust in central Italy from geophysical log data. *Scientific reports*, 10(1):3834, 2020.

Nicol, A., Walsh, J., Manzocchi, T., and Morewood, N. Displacement rates and average earthquake recurrence intervals on normal faults. *Journal of Structural Geology*, 27(3):541–551, 2005.

Niemeijer, A. R. and Collettini, C. Frictional properties of a low-angle normal fault under in situ conditions: Thermally-activated velocity weakening. *Pure and Applied Geophysics*, 171:2641–2664, 2014.

Noda, H., Dunham, E. M., and Rice, J. R. Earthquake ruptures with thermal weakening and the operation of major faults at low overall stress levels. *Journal of Geophysical Research: Solid Earth*, 114(B7), 2009.

Oeser, J., Bunge, H.-P., and Mohr, M. Cluster design in the earth sciences tethys. In *International conference on high performance computing and communications*, pages 31–40. Springer, 2006.

Palgunadi, K. H., Gabriel, A., Ulrich, T., López-Comino, J. , and Mai, P. M. Dynamic Fault Interaction during a Fluid-Injection-Induced Earthquake: The 2017 Mw 5.5 Pohang Event. *Bulletin of the Seismological Society of America*, 110(5):2328–2349, 08 2020. doi: 10.1785/0120200106.

Palgunadi, K. H., Gabriel, A.-A., Garagash, D. I., Ulrich, T., and Mai, P. M. Rupture dynamics of cascading earthquakes in a multiscale fracture network. *Journal of Geophysical Research: Solid Earth*, 129(3):e2023JB027578, 2024.

Palmer, A. C., Rice, J. R., and Hill, R. The growth of slip surfaces in the progressive failure of over-consolidated clay. *Proceedings of the Royal Society of London. A. Mathematical and Physical Sciences*, 332(1591):527–548, 1973. doi: 10.1098/rspa.1973.0040.

Pelties, C., De la Puente, J., Ampuero, J.-P., Brietzke, G. B., and Käser, M. Three-dimensional dynamic rupture simulation with a high-order discontinuous Galerkin method on unstructured tetrahedral meshes. *Journal of Geophysical Research: Solid Earth*, 117(B2), 2012.

Pelties, C., Gabriel, A.-A., and Ampuero, J.-P. Verification of an ADER-DG method for complex dynamic rupture problems. *Geoscientific Model Development*, 7(3):847–866, 2014. doi: 10.5194/gmd-7-847-2014.

Poggiali, G., Chiaraluce, L., Ross, Z. E., Zhu, W., and Marone, C. Source Mechanics of the Altotiberina Fault System from a High-Resolution Machine-Learning. *BSSA*, XX(XX):1–21, 2025. doi: 10.1785/0120250072.

Power, W., Tullis, T., Brown, S., Boitnott, G., and Scholz, C. Roughness of natural fault surfaces. *Geophysical Research Letters*, 14(1):29–32, 1987.

Ramos, M. D. and Huang, Y. How the transition region along the Cascadia megathrust influences coseismic behavior: Insights from 2-D dynamic rupture simulations. *Geophysical Research Letters*, 46(4):1973–1983, 2019.

Ramos, M. D., Huang, Y., Ulrich, T., Li, D., Gabriel, A.-A., and Thomas, A. M. Assessing margin-wide rupture behaviors along the Cascadia megathrust with 3-D dynamic rupture simulations. *Journal of Geophysical Research: Solid Earth*, 126(7):e2021JB022005, 2021.

Ramos, M. D., Thakur, P., Huang, Y., Harris, R. A., and Ryan, K. J. Working with dynamic earthquake rupture models: A practical guide. *Seismological Society of America*, 93(4):2096–2110, 2022.

Rekoske, J. M., Gabriel, A.-A., and May, D. A. Instantaneous Physics-Based Ground Motion Maps Using Reduced-Order Modeling. *Journal of Geophysical Research: Solid Earth*, 128(8):e2023JB026975, 2023.

Rice, J. R. Heating and weakening of faults during earthquake slip. *Journal of Geophysical Research: Solid Earth*, 111(B5), 2006.

Rietbrock, A., Tiberi, C., Scherbaum, F., and Lyon-Caen, H. Seismic slip on a low angle normal fault in the Gulf of Corinth: Evidence from high-resolution cluster analysis of microearthquakes. *Geophysical Research Letters*, 23(14):1817–1820, 1996.

Rodriguez Padilla, A. M., Oskin, M. E., Milliner, C. W., and Plesch, A. Accrual of widespread rock damage from the 2019 Ridgecrest earthquakes. *Nature Geoscience*, 15(3):222–226, 2022.

Rovida, A. N., Locati, M., CAMASSI, R. D., Lolli, B., and Gasperini, P. CPTI15, the 2015 version of the Parametric Catalogue of Italian Earthquakes. 2016.

Sibson, R. H. A note on fault reactivation. *Journal of Structural Geology*, 7(6):751–754, 1985.

Smith, S. and Faulkner, D. Laboratory measurements of the frictional properties of the Zuccale low-angle normal fault, Elba Island, Italy. *Journal of Geophysical Research: Solid Earth*, 115(B2), 2010.

Spencer, J. E. and Chase, C. G. Role of crustal flexure in initiation of low-angle normal faults and implications for structural evolution of the Basin and Range province. *Journal of Geophysical Research: Solid Earth*, 94(B2):1765–1775, 1989.

Taufiqurrahman, T., Gabriel, A.-A., Ulrich, T., Valentova, L., and Gallovič, F. Broadband dynamic rupture modeling with fractal fault roughness, frictional heterogeneity, viscoelasticity and topography: The 2016 Mw 6.2 Amatrice, Italy earthquake. *Geophysical Research Letters*, 49(22):e2022GL098872, 2022.

Taufiqurrahman, T., Gabriel, A.-A., Li, D., Ulrich, T., Li, B., Carena, S., Verdecchia, A., and Gallovič, F. Dynamics, interactions and delays of the 2019 Ridgecrest rupture sequence. *Nature*, 618(7964):308–315, 2023.

Tesei, T., Collettini, C., Carpenter, B. M., Viti, C., and Marone, C. Frictional strength and healing behavior of phyllosilicate-rich faults. *Journal of Geophysical Research: Solid Earth*, 117(B9), 2012.

Tinti, E., Casarotti, E., Ulrich, T., Taufiqurrahman, T., Li, D., and Gabriel, A.-A. Constraining families of dynamic models using geological, geodetic and strong ground motion data: The Mw 6.5, October 30th, 2016, Norcia earthquake, Italy. *Earth and Planetary Science Letters*, 576:117237, 2021.

Townend, J. and Zoback, M. D. Implications of earthquake focal mechanisms for the frictional strength of the San Andreas fault system. *Geological Society, London, Special Publications*, 186(1):13–21, 2001.

Ulrich, T., Gabriel, A.-A., Ampuero, J.-P., and Xu, W. Dynamic viability of the 2016 Mw 7.8 Kaikōura earthquake cascade on weak crustal faults. *Nature communications*, 10(1):1213, 2019.

Ulrich, T., Gabriel, A.-A., and Madden, E. H. Stress, rigidity and sediment strength control megathrust earthquake and tsunami dynamics. *Nature Geoscience*, 15(1):67–73, 2022.

Uphoff, C., Rettenberger, S., Bader, M., Madden, E. H., Ulrich, T., Wollherr, S., and Gabriel, A.-A. Extreme Scale Multi-Physics Simulations of the Tsunamigenic 2004 Sumatra Megathrust Earthquake. In *Proceedings of the International Conference for High Performance Computing, Networking, Storage and Analysis*, SC '17, New York, NY, USA, 2017. Association for Computing Machinery. doi: 10.1145/3126908.3126948.

Vadacca, L., Casarotti, E., Chiaraluce, L., and Cocco, M. On the mechanical behaviour of a low-angle normal fault: the Alto Tiberina fault (Northern Apennines, Italy) system case study. *Solid Earth*, 7(6):1537–1549, 2016. doi: 10.5194/se-7-1537-2016.

Valoroso, L., Chiaraluce, L., Di Stefano, R., and Monachesi, G. Mixed-mode slip behavior of the Altotiberina low-angle normal fault system

(Northern Apennines, Italy) through high-resolution earthquake locations and repeating events. *Journal of Geophysical Research: Solid Earth*, 122(12):10–220, 2017.

Visini, F., Meletti, C., Rovida, A., D'Amico, V., Pace, B., and Pondrelli, S. An updated area-source seismogenic model (MA4) for seismic hazard of Italy. *Natural Hazards and Earth System Sciences*, 22(8):2807–2827, 2022.

Vuan, A., Brondi, P., Sugan, M., Chiaraluce, L., Di Stefano, R., and Michele, M. Intermittent slip along the Alto Tiberina low-angle normal fault in central Italy. *Geophysical Research Letters*, 47(17):e2020GL089039, 2020.

Wallace, L. M., Ellis, S., Little, T., Tregoning, P., Palmer, N., Rosa, R., Stanaway, R., Oa, J., Nidkombu, E., and Kwazi, J. Continental breakup and UHP rock exhumation in action: GPS results from the W oodlark R ift, P apua N ew G uinea. *Geochemistry, Geophysics, Geosystems*, 15(11):4267–4290, 2014.

Webber, S., Norton, K., Little, T., Wallace, L., and Ellis, S. How fast can low-angle normal faults slip? Insights from cosmogenic exposure dating of the active Mai'iu fault, Papua New Guinea. *Geology*, 46(3):227–230, 2018.

Wernicke, B. Low-angle normal faults and seismicity: A review. *Journal of Geophysical Research: Solid Earth*, 100(B10):20159–20174, 1995.

Westaway, R. The mechanical feasibility of low-angle normal faulting. *Tectonophysics*, 308(4):407–443, 1999.

Wollherr, S., Gabriel, A.-A., and Mai, P. M. Landers 1992 "reloaded": Integrative dynamic earthquake rupture modeling. *Journal of Geophysical Research: Solid Earth*, 124(7):6666–6702, 2019.

Yin, A. Origin of regional, rooted low-angle normal faults: A mechanical model and its tectonic implications. *Tectonics*, 8(3):469–482, 1989.

Yin, A. Mechanisms for the formation of domal and basinal detachment faults: A three-dimensional analysis. *Journal of Geophysical Research: Solid Earth*, 96(B9):14577–14594, 1991.

Yu, H., Zhang, Z., Hu, F., Xu, D., and Chen, X. Estimation of the nucleation location and rupture extent of the 1850 Xichang, Sichuan, China, earthquake by dynamic rupture simulations on a multi-segment stepover structure. *Earth and Space Science*, 10(6):e2022EA002775, 2023.

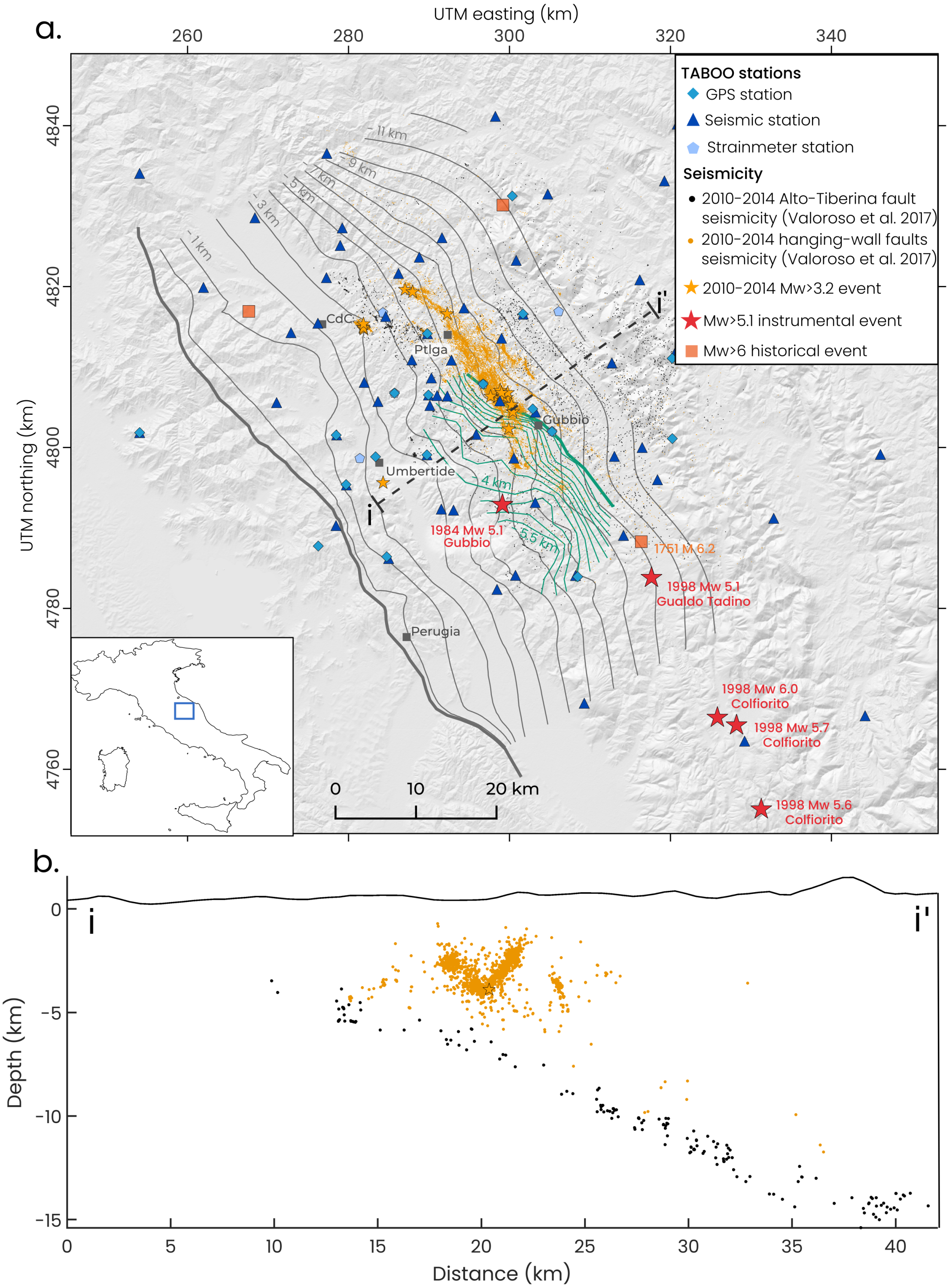

Figure 1 (a) Topographic map of the Alto Tiberina, Northern Apennines, Italy, area showing the depth contours of the north-east dipping Alto Tiberina (gray lines, Mirabella et al., 2011) and south-west dipping Gubbio (green lines, Mirabella et al., 2004) faults. Thicker lines indicate the fault surface traces. The black and orange dots show the 2010-2014 Alto-Tiberina and hanging wall faults seismicity, respectively (Valoroso et al., 2017). Note that, at the time this study was conducted, high-resolution catalogs published for the ATF fault system did not cover longer time periods. Light orange stars represent the Mw>3.2 events that occurred between 2010 and 2023 while large orange stars locate the large (Mw>5.1) instrumental events (Haessler et al., 1988; Chiaraluce et al., 2003; Ciaccio et al., 2006). Orange squares locate the M>6 historical events (Rovida et al., 2016). The GPS, seismic, and strainmeter stations of the TABOO-NFO (Chiaraluce et al., 2014) are shown by diamonds, triangles, and pentagons, respectively. Gray squares locate the main towns of the area. CdC and Ptlga mean Città di Castello and Pietralunga towns, respectively. The bottom-left inset shows the general location of the study area (blue box). The dashed line locates the cross-section shown in b. (b) Cross-section showing the seismicity on the Alto-Tiberina fault (black dots) and within its hanging wall (orange points and star). Events located within ±1 km of the cross-section are plotted.

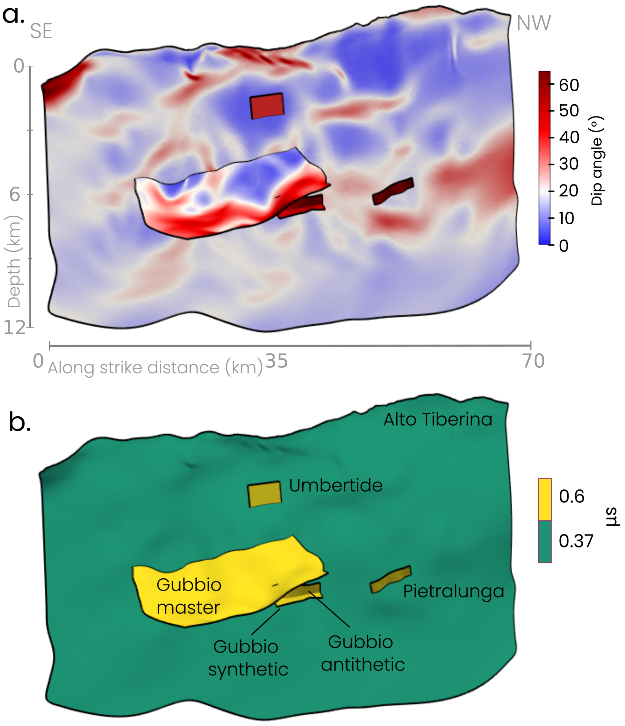

Figure 2 3D view of the modeled faults colored with (a) the dip angle and (b) the static friction coefficient used in our reference model. The colormap in panel (a) is chosen such that the low-angle areas of the fault (dip-angle < 20°) appear in bluish tones, while the steeper parts (dip angle > 20°) appear in reddish.

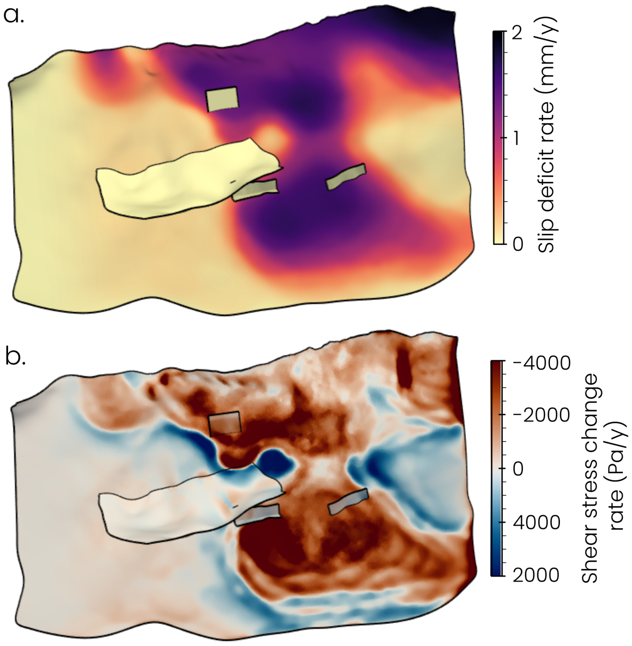

Figure 3 (a) Slip deficit rate on the Alto Tiberina fault computed from the kinematic coupling model of Anderlini et al. (2016) and (b) associated shear stress change rate.

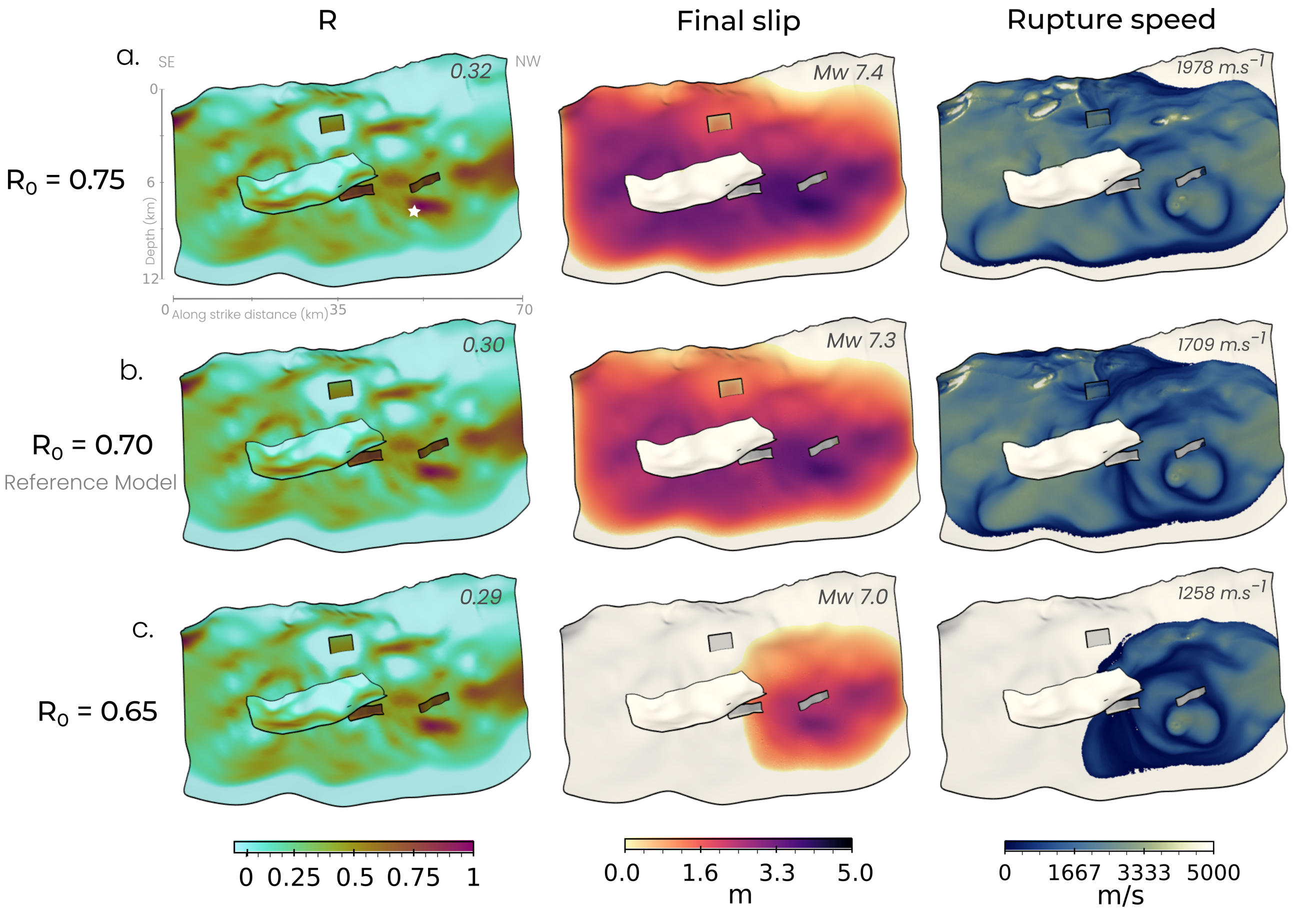

Figure 4 Influence of the pre-stress ratio R_0 on the homogeneous rupture scenarios. Distribution and average value of R ratio (left), final slip amplitude (middle), and rupture speed (right) for R_0 values of (a) 0.75, (b) 0.70, and (c) 0.65 respectively. The white star in the top left subplot shows the nucleation location (the nucleation location is the same for the three simulations). The average (and maximum) slip for R_0 values of 0.75, 0.70, and 0.65 is 2.2 m (4.4 m), 1.9 m (4.2 m), and 1.4 m (3.3 m), respectively.

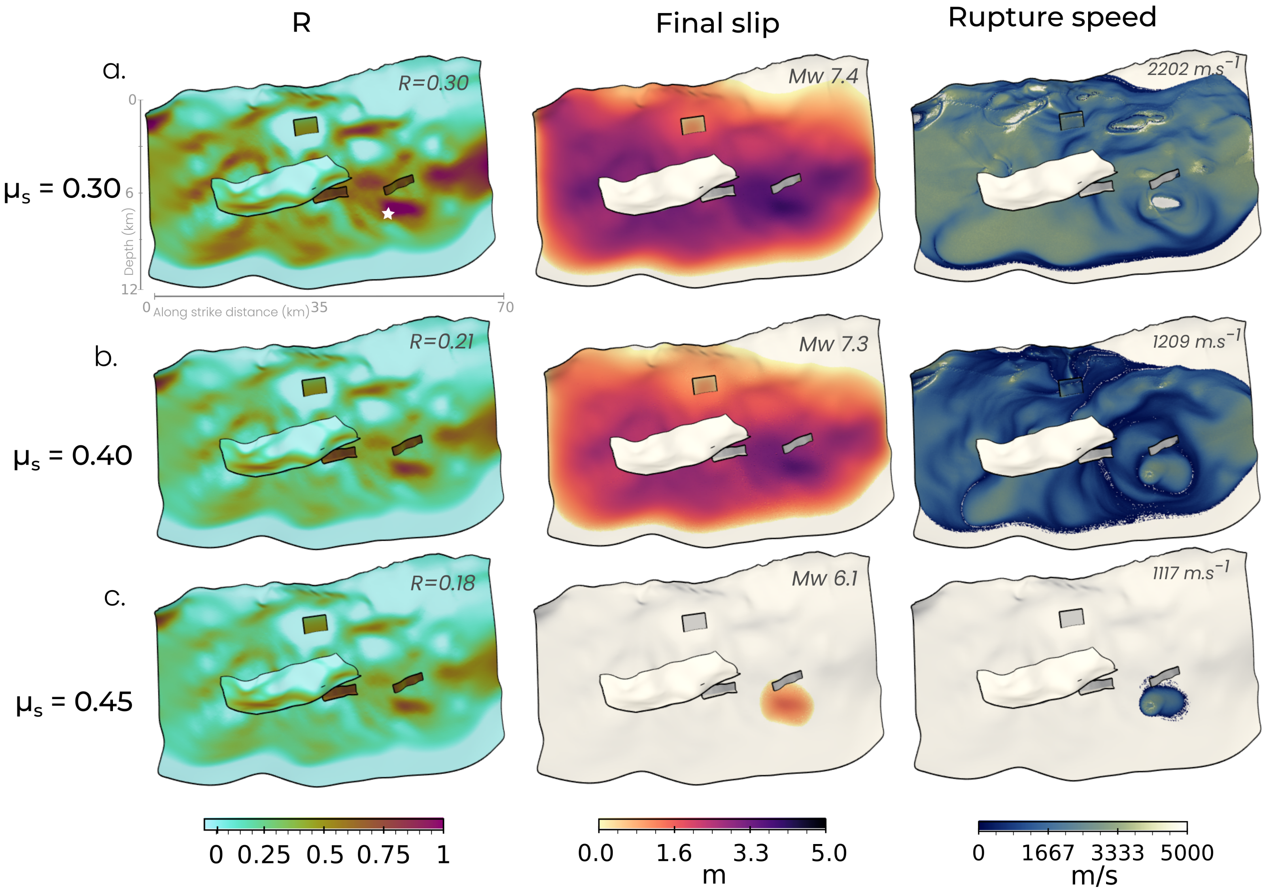

Figure 5 Influence of the the static friction coefficient μ_s of the Alto Tiberina fault on the homogeneous rupture scenarios. Distribution and average value of R ratio (left), final slip amplitude (middle), and rupture speed (right) for μ_s values of (a) 0.30, (b) 0.40, and (c) 0.45 respectively. R_0=0.70 for the three models. The white star in the top left subplot shows the nucleation location (the nucleation location is the same for the three simulations). The average (and maximum) slip for μ_s values of 0.30, 0.40, and 0.45 is 2.1 m (4.20 m), 1.8 m (4.3 m), and 0.7 m (1.50 m), respectively.

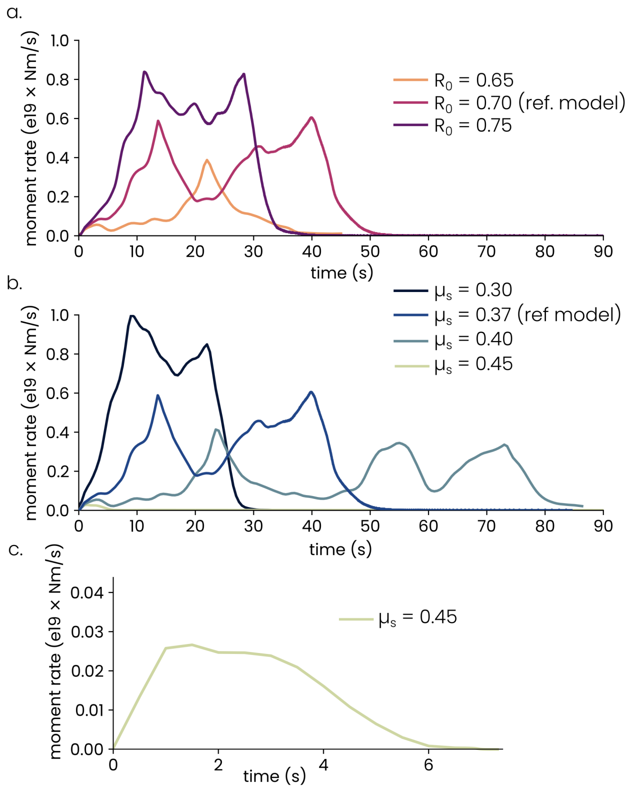

Figure 6 Impact of the (a) pre-stress level R_0 and (b) static friction coefficient μ_s of the Alto Tiberina fault on the moment rate release of the homogeneous scenarios. (c) Close-up view of the moment rate release for the model μ_s=0.45.

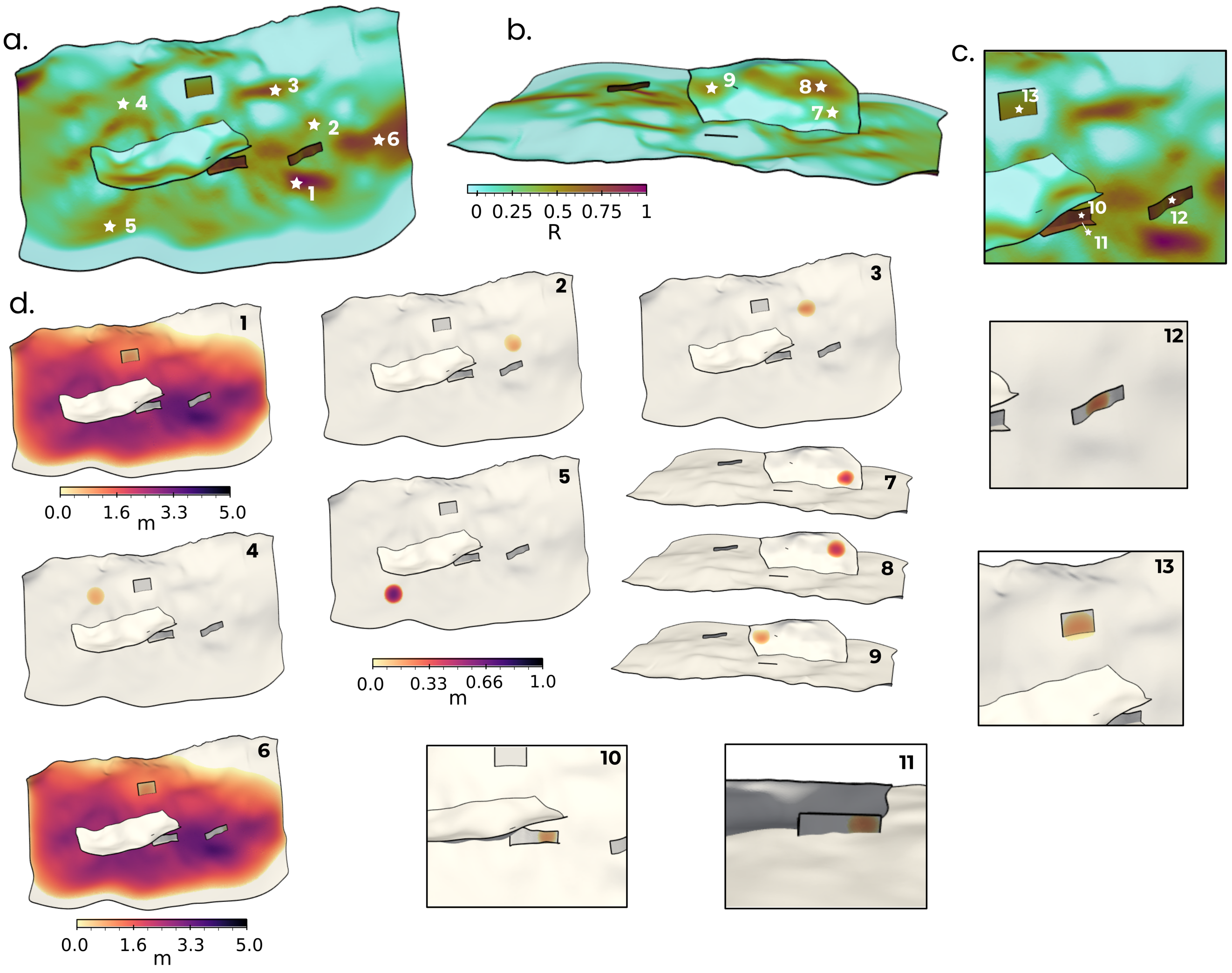

Figure 7 Impact of the nucleation location on the homogeneous scenario. (a) R ratio distribution of the reference homogeneous scenario (Table 1) and tested nucleation locations on the Alto Tiberina fault (white stars). (b,c) Same as (a) with a different view showing the tested nucleation locations on the Gubbio fault and on the secondary faults, respectively. (d) Final slip distribution for the different nucleation locations. The black number written on the top-right of each model corresponds to the nucleation location shown in Figure (a-c). The colorscale is between 0 and 5 m for the models 1 and 6 and between 0 and 1 m for the others. All the tests share the same initial conditions (R_0=0.70, μ_s = 0.37), only the nucleation location differs.

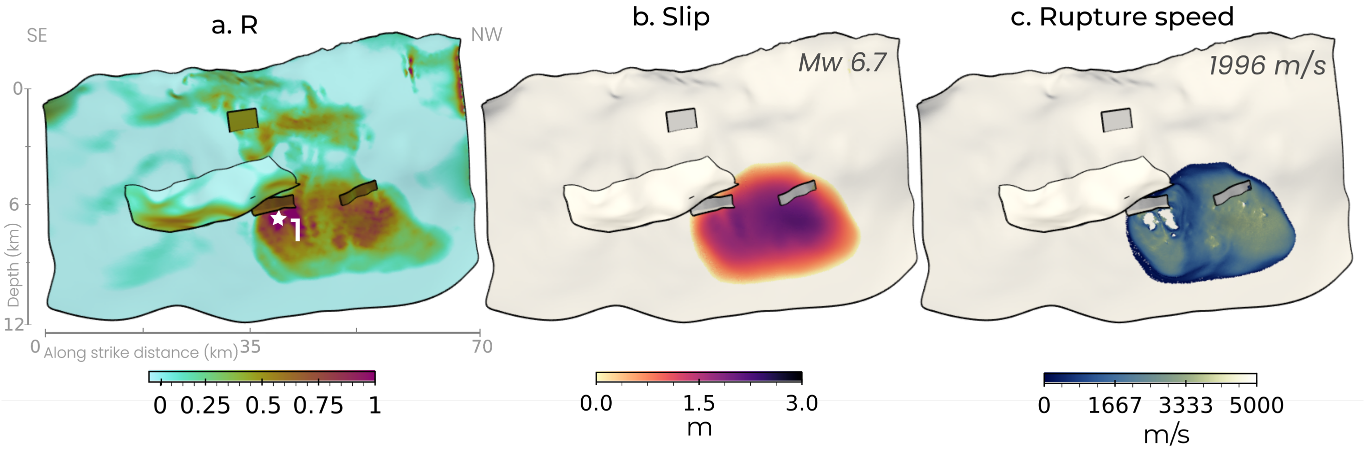

Figure 8 Data-constrained simulation. The initial stresses are constrained from the kinematic coupling map of Anderlini et al. (2016). The shear stress change computed from the slip deficit rate and assuming T=1800 years is added to an Andersonian background stress field having the same orientation and shape as in the homogeneous scenarios, but with a null pre-stress level (R_0=0). (a) Pre-stress level distribution, (b) final slip distribution and (c) rupture speed of the data-constrained model. The white star on panel (a) locates the nucleation location.

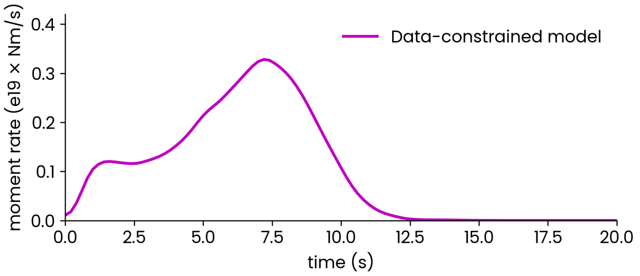

Figure 9 Moment rate release of the data-constrained simulation.

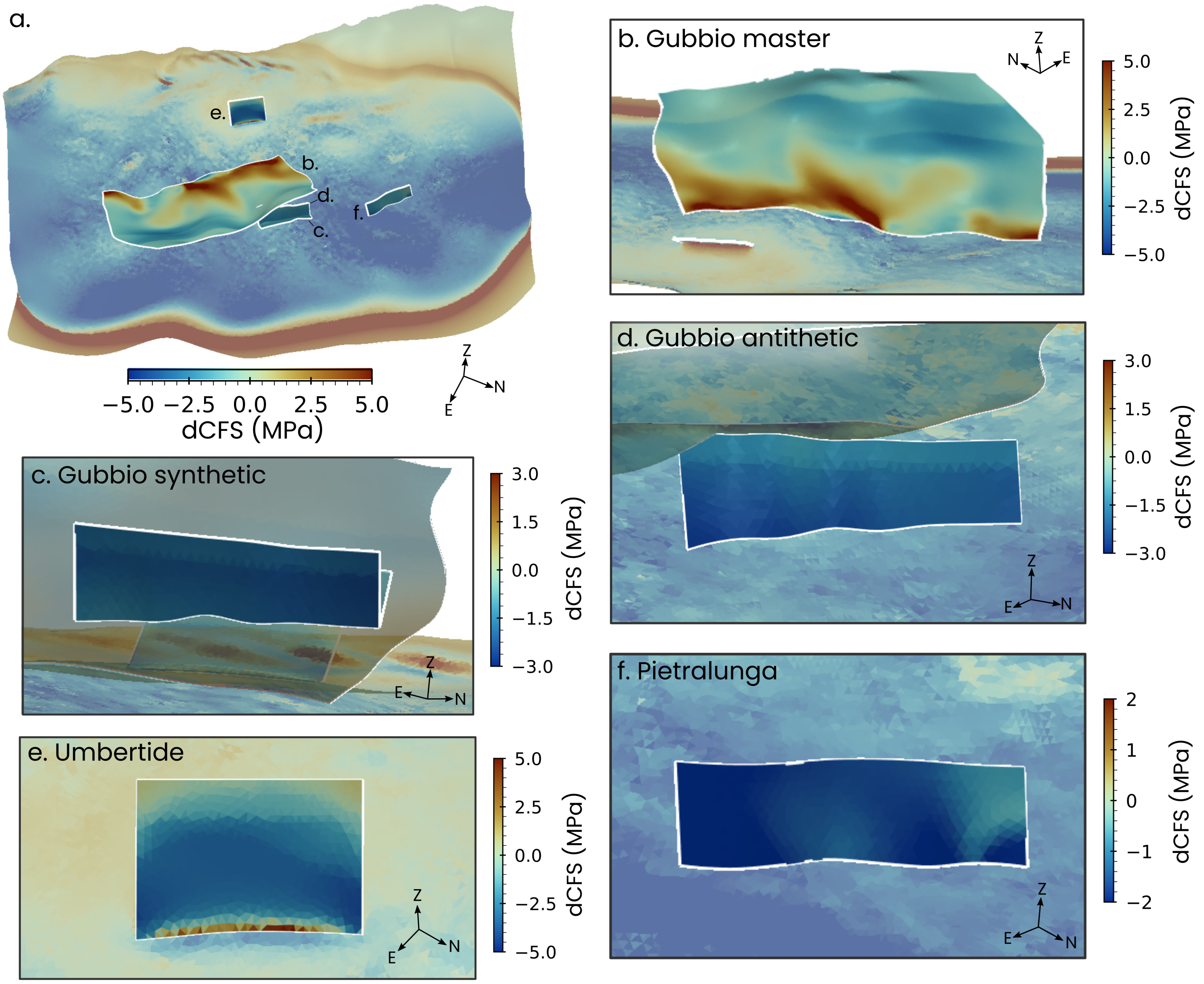

Figure 10 (a) Coulomb stress changes (dCFS) induced by the homogeneous reference scenario (Figure 4b and Table 1) on the Alto Tiberina fault system. The Alto Tiberina fault is plotted with a lower opacity level to highlight the hanging wall faults. (b-f) Close-up views on each hanging wall fault. On panel d, the Gubbio synthetic segment is not plotted for visibility. Note that the Coulomb stress changes on the Umbertide segment (panel e) are negative because this segment ruptures during the reference scenario.